MNRAS **000**, 1–?? (2016) Preprint 5 October 2016 Compiled using MNRAS LATEX style file v3.0

Herschel-ATLAS: Revealing dust build-up and decline across gas, dust and stellar mass selected samples: I. Scaling relations

P. De Vis[1,2⋆], L. Dunne[3,4], S. Maddox[3,4], H.L. Gomez[3], C.J.R. Clark[3], A.E. Bauer[5], S. Viaene[2], S.P. Schofield[3], M. Baes[2], A.J. Baker[6], N. Bourne[3], S.P. Driver[7], S. Dye[8], S.A. Eales[2], C. Furlanetto[8,9], R.J. Ivison[4,10], A.S.G. Robotham[7], K. Rowlands[11], D.J.B. Smith[12], M.W.L. Smith[2], E. Valiante[2], A.H. Wright[7]

[1]*Department of Physics & Astronomy, University of Canterbury, Private Bag 4800, Christchurch, New Zealand*
[2]*Sterrenkundig Observatorium, Universiteit Gent, Krijgslaan 281, B-9000 Gent, Belgium*
[3]*School of Physics & Astronomy, Cardiff University, Queen's Buildings, The Parade, Cardiff, CF24 3AA, UK*
[4]*Institute for Astronomy, The University of Edinburgh, Royal Observatory, Blackford Hill, Edinburgh, EH9 3HJ, UK*
[5]*Australian Astronomical Observatory, PO Box 915, North Ryde, NSW 1670, Australia*
[6]*Department of Physics and Astronomy, Rutgers, The State University of New Jersey, 136 Frelinghuysen Road, Piscataway, NJ 08854-8019, U.S.A.*
[7]*International Centre for Radio Astronomy Research, The University of Western Australia, Crawley, Perth, 6009, Australia*
[8]*School of Physics & Astronomy, University of Nottingham, University Park, Nottingham, NG7 2RD, UK*
[9]*CAPES Foundation, Ministry of Education of Brazil, Braslia/DF, 70040-020, Brazil*
[10]*European Southern Observatory, Karl Schwarzschild Strasse 2, Garching, D85748, Germany*
[11]*School of Physics & Astronomy, University of St Andrews, North Haugh, St Andrews, KY16 9SS, UK*
[12]*Centre for Astrophysics, Science & Technology Research Institute, University of Hertfordshire, Hatfield, Herts, AL10 9AB, UK*

arXiv:1610.01038v1 [astro-ph.GA] 4 Oct 2016

5 October 2016

ABSTRACT

We present a study of the dust, stars and atomic gas (HI) in an HI-selected sample of local galaxies ($z < 0.035$) in the *Herschel* Astrophysical Terahertz Large Area Survey (H-ATLAS) fields. This HI-selected sample reveals a population of very high gas fraction (> 80 per cent), low stellar mass sources that appear to be in the earliest stages of their evolution. We compare this sample with dust and stellar mass selected samples to study the dust and gas scaling relations over a wide range of gas fraction (proxy for evolutionary state of a galaxy). The most robust scaling relations for gas and dust are those linked to NUV-r (SSFR) and gas fraction, these do not depend on sample selection or environment. At the highest gas fractions, our additional sample shows the dust content is well below expectations from extrapolating scaling relations for more evolved sources, and dust is not a good tracer of the gas content. The specific dust mass for local galaxies peaks at a gas fraction of ~75 per cent. The atomic gas depletion time is also longer for high gas fraction galaxies, opposite to the trend found for molecular gas depletion timescale. We link this trend to the changing efficiency of conversion of HI to H_2 as galaxies increase in stellar mass surface density as they evolve. Finally, we show that galaxies start out barely obscured and increase in obscuration as they evolve, yet there is no clear and simple link between obscuration and global galaxy properties.

Key words: galaxies: evolution - galaxies: ISM - galaxies: fundamental parameters - galaxies: dwarf - ISM: dust, extinction - ISM: evolution

1 INTRODUCTION

About 30 to 50 per cent of the optical/UV radiative energy produced by stars and AGN in galaxies is absorbed by dust and thermally re-emitted in the Far-InfraRed (FIR) and submillimetre (submm) parts of the spectrum (Fixsen et al., 1996; Driver et al.,

⋆ E-mail: pieter.devis@pg.canterbury.ac.nz

© 2016 The Authors

2016; Viaene et al., 2016). It is therefore difficult to develop a thorough understanding of galaxy evolution without also understanding the InterStellar Medium (ISM). Dust properties have been investigated for several decades using space missions such as *IRAS* (Neugebauer et al., 1984), *ISO* (Kessler et al., 1996) and *Spitzer* (Werner et al., 2004) and ground based submillimetre instruments such as SCUBA (Holland et al., 1999), MAMBO (Kreysa et al., 1998) and LABOCA (Kreysa et al., 2003). However, with the advent of the *Herschel Space Observatory*[1] (Pilbratt et al., 2010) we have entered a new era for interstellar dust studies. *Herschel* has superior angular resolution and sensitivity compared to previous FIR facilities and operates right across the peak of the dust SED ($70-500\mu$m). This makes it sensitive to the diffuse cold ($T < 25$ K) dust component that dominates the dust mass in galaxies (Devereux et al., 1990; Dunne &Eales, 2001; Draine et al., 2007; Clark et al., 2015), as well as warmer ($T > 30$ K) dust radiating at shorter wavelengths which often dominates the dust luminosity. The consensus is that the warm dust component is heated by star-forming regions (Devereux &Young, 1990; Kennicutt, 1998; Calzetti et al., 2007; Boquien et al., 2010; Verley et al., 2010; Bendo et al., 2012), and the cold dust component (which makes up the bulk of the dust mass) can be heated by both star-forming regions and older stellar populations (Bendo et al., 2015).

Herschel is uniquely suited to studying the role played by dust in the evolutionary history of galaxies. The first logical step is to quantify how the dust content of galaxies varies with galactic properties such as stellar mass, colour, gas content, star formation rate (SFR), and other parameters. The resulting scaling relations provide vital information about the interplay of dust, gas and the star formation cycle, leading to important insights into the physical processes regulating galaxy evolution (e.g. Dunne et al., 2011) and providing strong constraints on chemical evolution models (e.g. Rowlands et al., 2014b; Zhukovska, 2014). Before *Herschel*, the main scaling relations studied were global relations between dust, gas and stellar masses (e.g. Devereux &Young, 1990; Sanders et al., 1991; Dunne et al., 2000; Driver et al., 2007) and the evolution of the dust-to-gas ratio with stellar mass and metallicity (e.g. Issa et al., 1990; Lisenfeld &Ferrara, 1998; James et al., 2002; Draine et al., 2007). These studies showed a strong correlation between dust and gas mass, and found an increase of the dust-to-gas mass ratio as a function of stellar mass and metallicity, though there is often disagreement in the exact slope of the relationships. More recently, da Cunha et al. (2010) used *IRAS* data to show that the dust-to-stellar mass ratio strongly correlates with specific star formation rate (SSFR), as predicted by chemical evolution models. This result has since been supported by further *Herschel* studies (Smith et al., 2012; Sandstrom et al., 2013; Rowlands et al., 2014a).

Since then, *Herschel* has expanded on these studies to include the cold dust component and explored a much wider range of galaxy types and luminosities, in far greater numbers, than was possible previously. The *Herschel* Reference survey (HRS, Boselli et al., 2010a) is a quasi stellar mass selected sample of 323 local galaxies. Various HRS studies have derived scaling relations between the gas, dust and star formation properties as well as trends with FIR/submm and UV colours, stellar mass, morphology and environment. Next to providing benchmark scaling relations, these works found cluster galaxies are characterized by a significantly lower atomic, molecular, and dust mass content than similar stellar mass galaxies in the field. (Cortese et al., 2011; 2012a;b; 2014; Boselli et al., 2012; 2013; 2014b; 2015). The *Herschel*-ATLAS (H-ATLAS, Eales et al., 2010) is a blind, large-area submm survey which provides an unbiased and unrivalled view of the nearby dusty Universe. Dust scaling relations in H-ATLAS have been studied by Bourne et al. (2012) through stacking $\sim$ 80000 optically selected galaxies and also by (Smith et al., 2011) who used fits to the UV-FIR photometry of 1402 250μm-selected sources. More recently H-ATLAS has produced a local volume limited sample, and Clark et al. (2015, hereafter C15) used it to study the dust properties of the first dust mass selected sample of galaxies in the local Universe.

C15 show that stellar mass selected samples are biased towards galaxies that have converted a lot of their gas into stars, i.e. towards more evolved galaxies, and thus under-represent immature high gas fraction sources. Dust selection produces a more uniform range of gas fractions but preferentially samples galaxies near the peak of their dust content. In this work we compare a local, HI-selected sample from the H-ATLAS equatorial fields to these stellar and dust mass selected samples. We will highlight scaling relations concerning dust properties as these have not been studied before for HI-selected samples. Since HI selection will bias us towards galaxies with high gas fractions, we can populate the scaling relations for these hitherto missing immature galaxies and, for the first time, study their dust properties. By comparing the three samples selected by stellar, dust and atomic gas content, we span a large range of gas fractions and can study the relationship of dust, gas and stars across as wide a range of evolutionary status as possible.

This paper is organized as follows. In Section 2 we describe the observations, the sample selection, the extended source photometry pipeline and the MAGPHYS SED fitting code that was used to obtain the galactic properties. In Section 3 we discuss the different surveys used in this work. In Section 4 we compare the dust, gas and stellar content of the HI, dust and stellar mass selected samples. In Section 5 we study the evolution of the star formation efficiency and in Section 6 we investigate the dust heating. Finally in Section 7 we study the obscuration for the different samples. We adopt the cosmology of Planck Collaboration et al. (2013), specifically $H_0 = 67.30\,\mathrm{kms}^{-1}\,\mathrm{Mpc}^{-1}$, $\Omega_\mathrm{m} = 0.315$, and $\Omega_\Lambda = 0.685$.

2 THE DATA

In order to obtain a sample of galaxies with sufficient multi-wavelength information to determine the stellar, dust and atomic gas (HI) content, it is necessary to select an area of sky which has been surveyed in the optical, in the submillimeter and at 21 cm. The ideal fields with the necessary multi-wavelength data are the three equatorial fields ($\sim$160 deg^2) of the *Herschel*-ATLAS (H-ATLAS; Eales et al., 2010) which have excellent multi-wavelength auxiliary data and overlap with the Galaxy And Mass Assembly spectroscopic survey (GAMA; Driver et al., 2009). The HI Parkes All-Sky Survey (HIPASS; Barnes et al., 2001), supplemented by the Arecibo Legacy Fast ALFA Survey (ALFALFA; Giovanelli et al., 2005) is used to determine the atomic gas properties.

2.1 Observations

The HI Parkes All Sky Survey (HIPASS; Barnes et al., 2001; Meyer et al., 2004) provides 21cm coverage over the equatorial H-ATLAS/GAMA fields. The Parkes beamsize is 15.5 arcmin, the velocity resolution is 18 km s^{-1} and the rms noise is 13 mJy beam^{-1}

[1] *Herschel* is an ESA space observatory with science instruments provided by European-led Principal Investigator consortia and with important participation from NASA.

in a channel of this width. The HIPASS catalogue (HICAT, Meyer et al., 2004; Zwaan et al., 2004; Wong et al., 2006) is used to identify our sources and extract the basic HI-parameters.

The HIPASS data are supplemented by observations from the Arecibo Legacy Fast ALFA Survey (ALFALFA, Giovanelli et al., 2005; Haynes et al., 2011; Haynes, *priv comm.*). With a beamsize of ~ 3.5 arcmin and rms noise of ~ 2 mJy beam^{-1} (for 11 km s^{-1} channels), ALFALFA outperforms HIPASS in both sensitivity and resolution. It does not however, have full coverage over the three equatorial H-ATLAS/GAMA fields in this study. For this reason we use HIPASS data supplemented with ALFALFA where available.

The uniqueness and strength of this HI-selected sample is that it makes use of the H-ATLAS - the largest extra-galactic submm survey covering ~ 600 deg^2 in 5 bands from 100-500 μm. The H-ATLAS observations were carried out in parallel mode using the Photodetector Array Camera and Spectrometer (PACS, Poglitsch et al., 2010) and the Spectral and Photometric Imaging REceiver (SPIRE, Griffin et al., 2010) instruments on board the *Herschel Space Observatory*. This work makes use of the H-ATLAS Phase 1 public data release, hereafter 'DR1' (Valiante et al., 2016; Bourne et al., 2016). (More details on the H-ATLAS data reduction can be found in Valiante et al. (2016).) To determine counterparts to our HI-selected sources, we use the DR1 catalogue of 4σ detections at 250 μm (Valiante et al., 2016) produced using the MAD-X algorithm (Maddox et al., *in prep.*). Optical counterparts to H-ATLAS sources were found by direct comparison with the SDSS DR7 (Abazajian et al., 2009) and DR9 (Ahn et al., 2012) by means of matching H-ATLAS sources to SDSS objects within a 10 arcsecond radius using a likelihood ratio technique, where only SDSS sources with a reliability R > 0.8 are considered to be likely matches to the H-ATLAS sources (Smith et al., 2011; Bourne et al., 2016).

For ultraviolet, optical and near-infrared data, we use images compiled by the Galaxy And Mass Assembly spectroscopic survey (GAMA; Driver et al., 2011; Hopkins et al., 2013; Liske et al., 2015). GAMA provides spectroscopic redshifts, along with supplementary reductions of ultraviolet (UV) *GALEX* (Morrissey et al., 2007; Seibert et al., 2012), optical SDSS DR6 (Adelman-McCarthy et al., 2008), Near-InfraRed (NIR) VISTA VIKING (Sutherland, 2012) and Mid-InfraRed (MIR) WISE (Wright et al., 2010; Cluver et al., 2014) data. Details of these reprocessed maps can be found in Driver et al. (2016).

Unfortunately we do not have CO data for our HI-selected sample so we cannot measure the molecular gas mass present in these galaxies. However, we have estimated molecular gas masses for our sources based on scaling relations from Saintonge et al. (2011) and Bothwell et al. (2014). We found that the estimated molecular gas component is small compared to the HI masses for HI-selected sources. Using these scaling relations to derive total (HI+H_2) gas masses instead of HI masses does not change the overall conclusions presented in this work.

2.2 Sample selection

Our sample consists of the 32 sources in the HIPASS catalogue (HICAT) that overlap with the H-ATLAS/GAMA footprints. These HI sources are cross-matched to the H-ATLAS DR1 catalogue and to SDSS DR9 (Ahn et al., 2012). The matching is done by identifying all optical and submm sources that lie within the $15.5'$ Parkes beam and have spectroscopic redshifts within the redshift-range of the HIPASS profile. To be accepted, optical matches need to have a reliable redshift from GAMA or SDSS and the H-ATLAS matches need to have a reliable SDSS counterpart (R > 0.8, Smith et al., 2011). The H-ATLAS matches are combined with their corresponding optical matches when possible.

We identified two additional sources by checking the literature for bright HI sources that are located in the H-ATLAS fields, but are not found by HIPASS. Both UGC0700 (Sulentic &Arp, 1983) and NGC5746 (Popping &Braun, 2011) were detected with Arecibo ($3.5'$ beam) and both are bright enough to be detected by HIPASS, yet lie just outside the beam of the closest HIPASS source (separation of about $20'$). The close proximity to another bright HIPASS source likely caused these sources to be missed. However they are still bright enough to meet our selection[2] and both these sources are added to our sample.

Multiple optical matches are found for 30 out of the 32 HIPASS sources due to two different issues. The first is that the SExtractor (Bertin &Arnouts, 1996) source detection used by SDSS and GAMA was not optimised for the very extended local sources in our sample (semi-major axis up to 3 arcmin). Most of the sources in our sample also have clumpy optical distributions, which together with their large angular sizes, leads to SExtractor 'shredding' galaxies into several components; 71 per cent of the sources in our sample are affected by this shredding. For these sources we determine the correct central position manually and reject the spurious listings. Fluxes were measured as described in Section 2.3.

After correcting the shredding issue, there are still a number of HIPASS sources that have multiple distinct galaxy matches. These galaxies are 'confused' in the large HI beam and there is no sure way of determining how much of the HI signal corresponds to each of the sources without obtaining higher angular resolution observations. The galaxies for which the HIPASS signal is confused are labelled 'a' in Tables B1 and B2. The projected physical distance between these confused galaxies is relatively small (~ 100 kpc) and they form groups (consisting of up to 5 sources). In total, there are 49 matches to the 32 HIPASS sources in the sample.

In order to better determine the HI properties for the confused sources, we have supplemented the HIPASS data with ALFALFA data where available ($3.5'$ beam size). ALFALFA only covers the more northern sources in the sample (dec $> -0.05°$) and we find an unconfused HI source for 23 out of the 49 optical matches. Because of its higher sensitivity, we use the ALFALFA HI measurements for all sources that lie in its footprint. The ALFALFA data resolves 3 of the 9 confused HIPASS sources into 7 separate HI sources, each with its own optical counterpart. We are then left with 6 confused HIPASS sources, containing 14 optical matches between them. For these we have searched the literature for the highest resolution 21 cm observations available, leading to the deconfusion of 5 HIPASS sources into 8 separate HI sources with optical counterparts (see Table B2 for relevant references). This leaves us with 1 HIPASS source for which there are two optical matches. For this source, we estimate which of the two candidate counterparts contributes the vast majority of the HI signal. The dominant source was chosen by comparing the stellar masses, the NUV-*r* colours and the offsets in optical positions and velocities of the optical counterparts from HIPASS. Based on these, we are confident that one counterpart (labelled 'b' in Table B1 and Table B2) has nearly all the HI mass, and the other is a small satellite galaxy that can be discarded together with all the other optical matches without HI detections. In Table 1, we present the key characteristics of the sources in our HI-selected sample, such as their common names, positions, red-

[2] Without the close proximity to another HIPASS source, both these sources would have been included in the HIPASS sample.

shifts, distances and sizes. Distances were calculated using spectroscopic redshifts using $H_0 = 67.30\,\mathrm{km\,s^{-1}\,Mpc^{-1}}$, with velocities corrected by GAMA (Baldry et al., 2012) to account for bulk deviations from Hubble flow[3] (Tonry et al., 2000). We use the standard prescription to determine HI masses:

$$M_{HI} = 2.356 \times 10^5\ S_{int}\ D^2$$

where M_{HI} is the HI mass in solar units, S_{int} is the integrated 21 cm line flux in Jy km s^{-1} and D is the Hubble flow corrected distance in Mpc. The HI-derived properties are listed in Table 2.

The HI fluxes and masses in Table B2 have not been corrected for self-absorption (which occurs if there is a high optical depth in the line of sight for HI clouds). Bourne et al. (2013) calculated this correction for a sample of 20 galaxies over the H-ATLAS fields. The average correction factor for the overlapping sources with our HI-selected sample is 1.09. Neither of the comparative samples used in this work (see Section 3) have been corrected for self-absorption. For this reason, and because of the uncertainty associated with the correction, we do not account for self-absorption in this work, but note that our gas masses, particularly for edge on galaxies, could therefore be underestimated.

Adding in higher resolution HI data for known HIPASS detections could affect our HI selection. Although we have found ALFALFA counterparts to each of the HIPASS sources in the common region, we cannot be confident that these individual counterparts would have made the HIPASS detection limit by itself. This is possibly an issue for the 3 sources in our sample with $S_{int} < 1.7$ Jy (labelled 'c' in Table 1) and we therefore ignore these when we discuss selection effects later. These sources do not change any of our conclusions, which is why we include them in our plots and do not discuss further. Finally we arrive at a sample of 40 unconfused HI-selected sources, 22 of which overlap with the C15 dust-selected sample (HAPLESS ID given in Table B1). Note that this is more than the original number of HIPASS sources due to the additional ALFALFA and literature data for the confused sources. These 40 sources will form our sample of 'HI-selected Galaxies in H-ATLAS', hereafter referred to as the HIGH sample.

2.3 Extended-source photometry

To study the extended galaxies in a consistent way across 21 bands ranging from FUV to 500μm, we consider the same physical area for each wavelength. We perform our own aperture-matched photometry across the entire UV-to-submm wavelength range, with exceptions for the IRAS 60 μm measurements and for the PACS 100 μm and 160 μm aperture fitting. The exceptions are described in Appendix A.

The first stage of the process consists of determining the appropriate aperture for each source. As described in C15, the optimal shape and size of the aperture are automatically determined in each band from FUV to 22μm and the largest aperture (after correcting the aperture size for the PSF) is selected as the definitive photometric aperture (typically FUV or NUV). The semi-major axes of the apertures used are listed in Table B1.

Next we removed bright foreground stars as decribed in C15, by using a curve of growth to measure the size of each star and then replacing stellar pixels with pixels randomly drawn from an annulus around the mask. In addition to this, a similar technique was used to remove background galaxies and remaining bright stars, yet using manually determined masking apertures. This was necessary for our HI-selected sample as many of the most HI-rich sources are low surface brightness and more susceptible to the effects of contaminating sources in the apertures.

After contaminant removal, the aperture matched photometry was performed in each band and the uncertainties determined. The photometry from the FUV to K_s-band was corrected for Galactic extinction in the same way as GAMA, using the method described in Adelman-McCarthy et al. (2008).

2.3.1 *Uncertainties*

The aperture noise for the UV-IR bands was estimated as in C15, using random apertures placed on non-target regions of the map and using a clipping procedure to mimic the effects of the star subtraction performed in the main target aperture and sky annulus. The aperture noise for *Herschel* was also estimated by placing random apertures, yet without additional clipping. Instead all extended sources in the H-ATLAS DR1 catalogue were masked using the H-ATLAS aperture and only randomly placed apertures not containing masked pixels were accepted.

Compared to C15, we include an additional source of uncertainty related to the accuracy of the star subtraction process. For each source and each band, we calculate the uncertainty as the average relative difference between the original photometry and photometry performed with a contaminant removal with stellar/galaxy radii that differ by ±10 per cent. This uncertainty is small for most sources but can dominate the total uncertainty for the few ($\sim$ 10 per cent of sample) sources with strong stellar contamination.

The above errors are added in quadrature to the aperture noise and the resulting photometry is given in Table B3 in Appendix B. Before fitting SEDs, we apply an additional term of uncertainty to account for the calibration uncertainty, model uncertainties in our SED fitting (see next Section) and contributions from spectral lines. For this additional term we use either 10 per cent or the calibration error, whichever is larger.

2.4 SED fitting

To interpret the resulting panchromatic SEDs of the galaxies in our HIGH sample in terms of their physical properties, we use the MAGPHYS code of da Cunha et al. (2008)[4]. MAGPHYS uses libraries of $\sim$ 50000 optical and $\sim$ 50000 infrared models to describe the stellar and dust SED respectively. These models are combined in such a way that the energy balance is maintained in both the diffuse ISM and the birth clouds. For each combination, the model SED is compared to the observed galaxy SED and a goodness-of-fit χ^2 calculated. Probability density functions (PDF) can then be made for any of the model physical parameters by weighting the value of that parameter by the probability $e^{\frac{-\chi^2}{2}}$. Our most reliable estimate for each parameter is the median value of its PDF and the corresponding uncertainties are the 16th and 84th percentiles of the PDF. For more details on the MAGPHYS models, we refer to da Cunha et al. (2008).

[3] C15 used a redshift-independent distance for NGC5584 from measurements of Cepheid variables (Riess et al., 2011). However there is a lot of scatter in redshift-independent distance estimates for NGC5584, and we have opted to use the same method as for the other sources in our sample.

[4] The MAGPHYS package containing the models of da Cunha et al. (2008) is publicly available at: www.iap.fr/magphys

We made some adaptations to MAGPHYS in order to tailor to our sample. These include:

– The cold dust temperature range needed to be extended to 10 - 30 K (instead of the standard 15 - 25 K) in order to fit some of the dusty sources in our sample.
– Some HIGH sources have bands with low SNR, and in some cases the measured fluxes in the FIR are negative, though with errors which are consistent with a zero or positive flux at the 1 sigma level. The standard MAGPHYS version does not deal with negative fluxes, yet we have incorporated them in our χ^2 calculation, as they still give statistical constraints.
– Additionally we added a routine that allows to include IRAS 60 μm upper limits (necessary for a third of our sample). For these upper limits, we only add a contribution to χ^2 if the model fluxes are higher than the upper limit flux.
– We have generated a PDF for the dust attenuation in the FUV (A_{FUV}) by comparing the attenuated and unattenuated model FUV fluxes for each model.

Before fitting the SEDs, we correct the SPIRE fluxes in Table B3 for K_{beam} and apply the additional uncertainty term to all bands (see Section 2.3.1). MAGPHYS intrinsically applies colour corrections to all fluxes, so the K_{colP} colour corrections from the SPIRE handbook do not need to be applied. The MAGPHYS results for the HIGH sample are presented in Table 1 and multiwavelength images and SEDs for HIGH are given in Figures B1 and B2 respectively.

3 SURVEYS USED IN THIS WORK

Here we introduce the dust-selected and stellar mass selected samples of local galaxies to compare with our HI-selected sample.

3.1 Dust-selected sample

The best comparative dust-selected sample is the *Herschel*-ATLAS Phase-1 Limited-Extent Spatial Survey (HAPLESS) described in the companion paper to this work (C15). HAPLESS is a volume limited sample consisting of 42 H-ATLAS galaxies detected at 250μm in the equatorial H-ATLAS fields with $0.0035 < z < 0.01$. Throughout the rest of this work we will refer to HAPLESS as a dust-selected sample to indicate this 250μm flux selection.

HAPLESS has 22 sources in common with HIGH and the photometry was performed using the same pipeline. For consistency, we have redetermined the *Herschel* photometry for HAPLESS using the H-ATLAS DR1 maps that have since become available. Additionally we redetermined the galaxy properties for HAPLESS using MAGPHYS instead of the combination of different techniques at different wavelengths used by C15. The MAGPHYS cold dust temperatures are, on average, 3 K warmer and the dust masses smaller by 0.25 dex than the results in C15, and the offset is largest for sources with cold ($T_c < 15$ K) dust temperature in C15. The differences originate in part from differences in the SED fitting technique and in part from changes to the *Herschel* photometry due to using the H-ATLAS DR1 data release instead of Phase 1 version 3. In contrast to modified blackbody fits in C15, MAGPHYS limits the warm dust to $30 < T_w < 60$ K, and at least half of the dust luminosity in the diffuse ISM must originate from the cold dust component. Therefore MAGPHYS assigns low probabilities to poorly constrained cold dust components that make up a tiny fraction of the total luminosity but peak at the longest wavelengths, therefore making up the bulk of the dust mass. Additionally, MAGPHYS uses the median Tc from the PDF whereas C15 used the best fit to the data; when comparing C15 with the best-fit MAGPHYS result, we find overall a better agreement between the two estimates. C15 compiled literature atomic gas masses, including HIPASS (Meyer et al., 2004) and ALFALFA (Haynes, *priv. comm.)*.

3.2 Stellar mass selected sample

For a stellar mass selected sample we follow C15 and use the *Herschel* Reference Survey (HRS, Boselli et al., 2010a) which targeted 323 local galaxies. The HRS is a volume-limited sample (between 15 and 25 Mpc) and uses K_S-band selection because this band suffers least from extinction and is known to be a good proxy for stellar mass; throughout the rest of this work, we will refer to the HRS as a stellar mass selected sample. The HRS contains both Late Type Galaxies (LTG) and 75 Early Type Galaxies (ETG) and includes many galaxies in cluster environments. We do not include ETGs when determining best fit relations and correlations. Instead we highlight them as a separate sub-sample in the plots.

Again, for consistency, we derived properties for HRS sources using MAGPHYS. Our results are slightly different to the MAGPHYS HRS results in Viaene et al. (2016) because they did not apply any corrections for galactic extinction and K_{beam}, and used smaller uncertainties. For the HI masses of the HRS galaxies, we used the unconfused results from Boselli et al. (2014a). For HRS, CO derived H_2 masses are presented in Boselli et al. (2014a) and can be relatively large compared to their HI. However, they are still small compared to the total baryon mass and using total (HI+H_2) gas masses instead of HI masses only gives small differences to the overall scaling relations for HRS in this work.

4 DUST, GAS AND STARS

We first investigate the distribution of the relative masses of stars, dust and atomic gas. The distribution of the gas fractions ($\frac{M_{HI}}{M_*+M_{HI}}$) in the left panel of Figure 1 shows that the HIGH sample is more gas rich than the HRS, while the HAPLESS gas fractions are relatively uniformly distributed. In this paper, we will define the evolutionary status of a galaxy using its gas fraction as a measure of how much of the available gas reservoir has been converted into stars[5]. HRS then consists mainly of evolved sources, HAPLESS consists of galaxies at a range of stages of evolution and the HIGH *sample consists mainly of relatively unevolved sources*. Our HI selection therefore gives us vital insights into the 'youthful' sources which were previously under-represented in samples like the HRS.

Figure 1 also shows that the specific dust mass (M_d/M_*) is highest for HAPLESS, followed by HIGH and then HRS. When we look at the distribution of dust-to-HI ratio we now find that HIGH has the lowest M_d/M_{HI}, followed by HAPLESS and then HRS. Finally we show the NUV-*r* colour distribution in the right panel of Figure 1. This colour is closely related to the specific star formation rate and we find that both the HAPLESS and HIGH samples are much bluer and thus more actively forming stars than the HRS. The large tail of red sources in HRS is because it contains a larger fraction of more evolved, passive sources.

[5] The most important caveat to this method is that we do not take into account interactions like inflows, outflows and merging.

Table 1. Properties of the 40 HiGH sources derived with MAGPHYS SED fitting. The columns are (from left to right): Index, galaxy name, stellar mass, dust luminosity, dust mass, M_d/M_*, temperature of the cold dust component, star formation rate (SFR) averaged over the last 10^8 years, specific star formation rate (SSFR) averaged over the last 10^8 years, f_μ (the fraction of the total dust luminosity contributed by the diffuse ISM), and the FUV attenuation by dust. Uncertainties are indicated by the 84th-16th percentile range from each of the individual PDF.

#	Name	log M_* ($M_\odot$)	log L_d ($L_\odot$)	log M_d ($M_\odot$)	log M_d/M_*	T_c (K)	log SFR ($M_\odot\,yr^{-1}$)	log SSFR (yr^{-1})	f_μ	A_{FUV} (mag)
1	SDSSJ08...	$9.84^{+0.13}_{-0.13}$	$9.80^{+0.12}_{-0.15}$	$7.21^{+0.40}_{-0.41}$	$-2.63^{+0.42}_{-0.43}$	$16.1^{+4.2}_{-3.3}$	$-0.03^{+0.10}_{-0.13}$	$-9.88^{+0.16}_{-0.18}$	$0.81^{+0.20}_{-0.23}$	$0.29^{+0.19}_{-0.14}$
2[a]	UGC04673	$9.12^{+0.20}_{-0.17}$	$9.15^{+0.10}_{-0.14}$	$7.40^{+0.23}_{-0.27}$	$-1.74^{+0.28}_{-0.29}$	$12.5^{+2.1}_{-1.4}$	$-0.24^{+0.04}_{-0.05}$	$-9.36^{+0.18}_{-0.21}$	$0.34^{+0.07}_{-0.07}$	$0.49^{+0.37}_{-0.21}$
3	UGC04684	$9.35^{+0.14}_{-0.15}$	$9.40^{+0.07}_{-0.10}$	$6.70^{+0.16}_{-0.14}$	$-2.64^{+0.22}_{-0.21}$	$17.5^{+1.9}_{-2.0}$	$-0.36^{+0.10}_{-0.12}$	$-9.72^{+0.18}_{-0.19}$	$0.61^{+0.17}_{-0.13}$	$0.36^{+0.19}_{-0.13}$
4	UGC04996	$9.36^{+0.12}_{-0.10}$	$9.61^{+0.05}_{-0.06}$	$7.18^{+0.21}_{-0.19}$	$-2.18^{+0.25}_{-0.24}$	$14.8^{+2.5}_{-2.1}$	$-0.17^{+0.06}_{-0.06}$	$-9.53^{+0.12}_{-0.13}$	$0.69^{+0.07}_{-0.10}$	$0.23^{+0.16}_{-0.14}$
5	UGC06578	$8.02^{+0.10}_{-0.06}$	$8.68^{+0.04}_{-0.07}$	$5.72^{+0.32}_{-0.29}$	$-2.31^{+0.30}_{-0.32}$	$16.1^{+2.9}_{-2.5}$	$-1.02^{+0.03}_{-0.04}$	$-9.04^{+0.06}_{-0.11}$	$0.51^{+0.07}_{-0.07}$	$0.16^{+0.12}_{-0.05}$
6[a]	UGC06780	$9.00^{+0.18}_{-0.12}$	$8.85^{+0.04}_{-0.06}$	$6.97^{+0.20}_{-0.23}$	$-2.06^{+0.20}_{-0.24}$	$12.8^{+1.7}_{-1.2}$	$-0.36^{+0.11}_{-0.11}$	$-9.36^{+0.16}_{-0.21}$	$0.24^{+0.05}_{-0.00}$	$0.41^{+0.10}_{-0.10}$
7[a]	UM456	$8.28^{+0.15}_{-0.15}$	$8.64^{+0.10}_{-0.12}$	$4.96^{+0.59}_{-0.45}$	$-3.33^{+0.60}_{-0.46}$	$22.4^{+5.0}_{-5.8}$	$-0.76^{+0.04}_{-0.04}$	$-9.04^{+0.15}_{-0.16}$	$0.34^{+0.07}_{-0.07}$	$0.18^{+0.06}_{-0.14}$
8	UM456A	$7.88^{+0.11}_{-0.13}$	$8.30^{+0.21}_{-0.33}$	$4.89^{+0.65}_{-0.55}$	$-2.98^{+0.65}_{-0.56}$	$20.7^{+6.0}_{-5.8}$	$-1.32^{+0.12}_{-0.09}$	$-9.19^{+0.17}_{-0.14}$	$0.49^{+0.23}_{-0.25}$	$0.19^{+0.13}_{-0.12}$
9[a]	UGC06903	$9.89^{+0.09}_{-0.15}$	$9.48^{+0.04}_{-0.03}$	$7.17^{+0.10}_{-0.09}$	$-2.68^{+0.17}_{-0.14}$	$16.4^{+1.0}_{-1.1}$	$-0.24^{+0.04}_{-0.04}$	$-10.13^{+0.16}_{-0.10}$	$0.56^{+0.03}_{-0.03}$	$0.58^{+0.23}_{-0.11}$
10	UGC06970	$9.39^{+0.12}_{-0.15}$	$8.89^{+0.14}_{-0.18}$	$6.52^{+0.35}_{-0.51}$	$-2.86^{+0.39}_{-0.54}$	$14.6^{+3.6}_{-2.5}$	$-0.86^{+0.10}_{-0.12}$	$-10.26^{+0.18}_{-0.16}$	$0.56^{+0.25}_{-0.20}$	$0.32^{+0.14}_{-0.16}$
11	NGC4030b	$8.85^{+0.16}_{-0.14}$	$8.63^{+0.13}_{-0.20}$	$5.64^{+0.53}_{-0.44}$	$-3.22^{+0.55}_{-0.47}$	$19.9^{+5.6}_{-5.6}$	$-0.98^{+0.09}_{-0.32}$	$-9.83^{+0.16}_{-0.35}$	$0.39^{+0.13}_{-0.15}$	$0.32^{+0.41}_{-0.17}$
12	NGC4030	$10.88^{+0.12}_{-0.09}$	$10.88^{+0.03}_{-0.02}$	$7.96^{+0.04}_{-0.08}$	$-2.93^{+0.10}_{-0.14}$	$20.9^{+0.8}_{-0.5}$	$0.78^{+0.04}_{-0.05}$	$-10.10^{+0.10}_{-0.13}$	$1.96^{+0.10}_{-0.10}$	$0.55^{+0.04}_{-0.05}$
13[a]	UGC07053	$8.19^{+0.18}_{-0.10}$	$7.98^{+0.33}_{-0.34}$	$4.80^{+0.56}_{-0.54}$	$-3.41^{+0.58}_{-0.57}$	$23.2^{+4.5}_{-6.3}$	$-1.03^{+0.06}_{-0.07}$	$-9.22^{+0.12}_{-0.19}$	$0.19^{+0.15}_{-0.10}$	$0.71^{+0.23}_{-0.54}$
14[a]	UGC07332	$7.70^{+0.14}_{-0.13}$	$7.78^{+0.18}_{-0.28}$	$4.31^{+0.48}_{-0.40}$	$-3.40^{+0.50}_{-0.42}$	$24.1^{+4.2}_{-6.5}$	$-1.39^{+0.04}_{-0.04}$	$-9.09^{+0.13}_{-0.15}$	$0.19^{+0.07}_{-0.07}$	$0.27^{+0.66}_{-0.13}$
15	NGC4202	$10.30^{+0.11}_{-0.10}$	$10.29^{+0.03}_{-0.03}$	$7.46^{+0.07}_{-0.06}$	$-2.81^{+0.11}_{-0.14}$	$20.3^{+0.8}_{-0.8}$	$0.05^{+0.06}_{-0.17}$	$-10.25^{+0.11}_{-0.20}$	$1.74^{+0.10}_{-0.07}$	$0.67^{+0.11}_{-0.05}$
16	FGC1412	$6.94^{+0.13}_{-0.10}$	$7.33^{+0.20}_{-0.41}$	$3.84^{+0.78}_{-0.53}$	$-3.11^{+0.78}_{-0.55}$	$21.3^{+6.0}_{-7.3}$	$-2.43^{+0.14}_{-0.17}$	$-9.37^{+0.17}_{-0.21}$	$0.69^{+0.25}_{-0.38}$	$0.18^{+0.21}_{-0.10}$
17[a]	CGCG014-010	$7.29^{+0.13}_{-0.12}$	$6.88^{+0.34}_{-0.23}$	$3.48^{+0.45}_{-0.40}$	$-3.82^{+0.47}_{-0.39}$	$25.0^{+3.5}_{-5.8}$	$-2.14^{+0.04}_{-0.04}$	$-9.42^{+0.12}_{-0.14}$	$0.14^{+0.13}_{-0.05}$	$0.57^{+0.30}_{-0.48}$
18	UGC07394	$8.93^{+0.14}_{-0.12}$	$8.70^{+0.17}_{-0.13}$	$6.87^{+0.21}_{-0.23}$	$-2.07^{+0.24}_{-0.27}$	$12.2^{+1.7}_{-1.3}$	$-1.22^{+0.17}_{-0.34}$	$-10.15^{+0.21}_{-0.36}$	$0.69^{+0.28}_{-0.17}$	$0.39^{+0.23}_{-0.19}$
19[a]	UGC07531	$8.60^{+0.15}_{-0.08}$	$8.98^{+0.09}_{-0.18}$	$6.49^{+0.39}_{-0.39}$	$-2.13^{+0.41}_{-0.42}$	$13.7^{+3.5}_{-2.6}$	$-0.38^{+0.04}_{-0.04}$	$-8.97^{+0.09}_{-0.16}$	$0.26^{+0.07}_{-0.07}$	$0.16^{+0.16}_{-0.05}$
20	UM501	$7.90^{+0.10}_{-0.10}$	$8.65^{+0.24}_{-0.09}$	$5.10^{+0.71}_{-0.54}$	$-2.80^{+0.72}_{-0.53}$	$19.4^{+6.9}_{-5.6}$	$-1.06^{+0.12}_{-0.04}$	$-8.95^{+0.15}_{-0.11}$	$0.54^{+0.28}_{-0.07}$	$0.10^{+0.09}_{-0.04}$
21[a]	NGC5496	$9.46^{+0.14}_{-0.05}$	$9.51^{+0.04}_{-0.04}$	$7.12^{+0.14}_{-0.11}$	$-2.35^{+0.13}_{-0.14}$	$16.9^{+1.3}_{-2.0}$	$-0.23^{+0.04}_{-0.04}$	$-9.69^{+0.06}_{-0.14}$	$0.61^{+0.00}_{-0.10}$	$0.66^{+0.00}_{-0.37}$
22[a]	NGC5584	$9.97^{+0.09}_{-0.16}$	$10.04^{+0.04}_{-0.02}$	$7.51^{+0.07}_{-0.10}$	$-2.45^{+0.14}_{-0.15}$	$17.0^{+1.5}_{-1.2}$	$0.26^{+0.04}_{-0.04}$	$-9.71^{+0.16}_{-0.10}$	$0.79^{+0.13}_{-0.03}$	$0.39^{+0.40}_{-0.13}$
23	UGC09215	$9.31^{+0.14}_{-0.04}$	$9.57^{+0.02}_{-0.05}$	$6.95^{+0.09}_{-0.10}$	$-2.38^{+0.12}_{-0.16}$	$17.4^{+0.9}_{-1.5}$	$-0.24^{+0.02}_{-0.06}$	$-9.55^{+0.04}_{-0.15}$	$0.66^{+0.07}_{-0.05}$	$0.37^{+0.08}_{-0.06}$
24	2MASXJ14...	$9.60^{+0.13}_{-0.07}$	$9.98^{+0.07}_{-0.08}$	$7.26^{+0.18}_{-0.15}$	$-2.36^{+0.21}_{-0.19}$	$17.7^{+1.7}_{-2.1}$	$-0.03^{+0.07}_{-0.07}$	$-9.63^{+0.11}_{-0.14}$	$1.54^{+0.17}_{-0.15}$	$0.36^{+0.07}_{-0.06}$
25	IC1011	$10.16^{+0.13}_{-0.07}$	$10.59^{+0.04}_{-0.05}$	$7.41^{+0.08}_{-0.09}$	$-2.77^{+0.13}_{-0.14}$	$21.9^{+1.3}_{-1.2}$	$0.60^{+0.06}_{-0.04}$	$-9.56^{+0.09}_{-0.14}$	$1.66^{+0.13}_{-0.15}$	$0.40^{+0.10}_{-0.07}$
26	IC1010	$10.82^{+0.08}_{-0.25}$	$10.29^{+0.04}_{-0.02}$	$7.93^{+0.12}_{-0.13}$	$-2.85^{+0.21}_{-0.20}$	$16.1^{+1.4}_{-0.9}$	$0.44^{+0.04}_{-0.06}$	$-10.38^{+0.25}_{-0.10}$	$0.69^{+0.10}_{-0.07}$	$0.52^{+0.05}_{-0.15}$
27[a]	UGC09299	$8.61^{+0.19}_{-0.04}$	$8.82^{+0.03}_{-0.01}$	$6.39^{+0.15}_{-0.14}$	$-2.24^{+0.18}_{-0.20}$	$17.3^{+1.4}_{-1.4}$	$-0.55^{+0.04}_{-0.04}$	$-9.16^{+0.05}_{-0.20}$	$0.31^{+0.03}_{-0.00}$	$0.62^{+0.14}_{-0.04}$
28[a]	SDSSJ14...	$7.77^{+0.19}_{-0.18}$	$7.66^{+0.35}_{-0.41}$	$4.52^{+0.73}_{-0.63}$	$-3.24^{+0.76}_{-0.68}$	$21.3^{+5.9}_{-6.9}$	$-1.69^{+0.04}_{-0.04}$	$-9.46^{+0.19}_{-0.19}$	$0.26^{+0.28}_{-0.15}$	$0.31^{+0.54}_{-0.19}$
29	NGC5690	$10.38^{+0.11}_{-0.09}$	$10.48^{+0.03}_{-0.02}$	$7.61^{+0.05}_{-0.05}$	$-2.78^{+0.12}_{-0.12}$	$20.5^{+0.6}_{-0.8}$	$0.31^{+0.05}_{-0.04}$	$-10.07^{+0.10}_{-0.12}$	$2.59^{+0.10}_{-0.10}$	$0.59^{+0.05}_{-0.03}$
30	NGC5691	$10.01^{+0.10}_{-0.17}$	$10.15^{+0.03}_{-0.04}$	$6.85^{+0.07}_{-0.04}$	$-3.15^{+0.17}_{-0.14}$	$24.1^{+0.4}_{-1.2}$	$-0.06^{+0.06}_{-0.05}$	$-10.07^{+0.18}_{-0.11}$	$1.76^{+0.13}_{-0.10}$	$0.60^{+0.03}_{-0.04}$
31[a]	UGC09432	$8.19^{+0.02}_{-0.14}$	$7.76^{+0.17}_{-0.94}$	$4.40^{+0.48}_{-0.51}$	$-3.76^{+0.51}_{-0.53}$	$24.4^{+3.9}_{-6.0}$	$-1.06^{+0.05}_{-0.06}$	$-9.24^{+0.15}_{-0.06}$	$0.09^{+0.05}_{-0.07}$	$0.58^{+0.20}_{-0.50}$
32[a]	NGC5705	$9.33^{+0.08}_{-0.12}$	$9.34^{+0.01}_{-0.03}$	$7.35^{+0.12}_{-0.13}$	$-1.98^{+0.17}_{-0.15}$	$14.3^{+1.1}_{-1.3}$	$-0.24^{+0.04}_{-0.04}$	$-9.58^{+0.12}_{-0.09}$	$0.41^{+0.03}_{-0.03}$	$0.54^{+0.23}_{-0.16}$
33	NGC5725	$9.13^{+0.08}_{-0.13}$	$9.14^{+0.07}_{-0.09}$	$6.45^{+0.19}_{-0.19}$	$-2.68^{+0.21}_{-0.20}$	$17.3^{+2.6}_{-2.2}$	$-0.65^{+0.07}_{-0.07}$	$-9.78^{+0.14}_{-0.10}$	$0.71^{+0.10}_{-0.15}$	$0.32^{+0.14}_{-0.11}$
34	NGC5713	$10.56^{+0.14}_{-0.11}$	$10.94^{+0.03}_{-0.03}$	$7.54^{+0.05}_{-0.05}$	$-3.02^{+0.12}_{-0.14}$	$24.8^{+0.6}_{-0.9}$	$0.72^{+0.06}_{-0.05}$	$-9.84^{+0.12}_{-0.15}$	$2.71^{+0.10}_{-0.13}$	$0.57^{+0.04}_{-0.03}$
35	NGC5719	$10.79^{+0.09}_{-0.08}$	$10.45^{+0.03}_{-0.04}$	$7.43^{+0.07}_{-0.06}$	$-3.36^{+0.12}_{-0.11}$	$22.0^{+0.8}_{-1.0}$	$-0.17^{+0.04}_{-0.06}$	$-10.96^{+0.09}_{-0.11}$	$3.06^{+0.10}_{-0.17}$	$0.78^{+0.02}_{-0.02}$
36	UGC09482	$8.72^{+0.10}_{-0.14}$	$8.55^{+0.12}_{-0.15}$	$6.09^{+0.31}_{-0.27}$	$-2.62^{+0.32}_{-0.29}$	$15.5^{+2.6}_{-2.6}$	$-1.30^{+0.14}_{-0.18}$	$-10.02^{+0.19}_{-0.21}$	$0.56^{+0.17}_{-0.13}$	$0.29^{+0.31}_{-0.12}$
37[a]	UGC09470	$8.90^{+0.07}_{-0.13}$	$8.86^{+0.03}_{-0.03}$	$6.22^{+0.17}_{-0.19}$	$-2.65^{+0.16}_{-0.17}$	$18.2^{+2.3}_{-1.8}$	$-0.68^{+0.04}_{-0.04}$	$-9.58^{+0.13}_{-0.09}$	$0.39^{+0.07}_{-0.03}$	$0.50^{+0.16}_{-0.24}$
38	NGC5740	$10.28^{+0.11}_{-0.07}$	$10.03^{+0.04}_{-0.04}$	$7.16^{+0.07}_{-0.07}$	$-3.13^{+0.12}_{-0.10}$	$19.9^{+0.8}_{-0.9}$	$-0.05^{+0.04}_{-0.04}$	$-10.33^{+0.08}_{-0.12}$	$1.54^{+0.10}_{-0.13}$	$0.50^{+0.11}_{-0.05}$
39[a]	UGC07000	$9.11^{+0.08}_{-0.16}$	$9.15^{+0.07}_{-0.04}$	$6.43^{+0.12}_{-0.11}$	$-2.67^{+0.17}_{-0.14}$	$18.6^{+1.8}_{-1.5}$	$-0.45^{+0.04}_{-0.04}$	$-9.56^{+0.16}_{-0.09}$	$0.49^{+0.07}_{-0.13}$	$0.48^{+0.20}_{-0.25}$
40	NGC5746	$11.31^{+0.07}_{-0.10}$	$10.34^{+0.02}_{-0.01}$	$8.00^{+0.07}_{-0.07}$	$-3.30^{+0.10}_{-0.10}$	$17.1^{+0.4}_{-0.5}$	$-0.41^{+0.36}_{-0.70}$	$-11.72^{+0.37}_{-0.71}$	$1.46^{+0.10}_{-0.38}$	$0.87^{+0.08}_{-0.12}$
Mean		9.20	9.22	6.40	–2.80	18.9	–0.51	–9.71	0.43	0.86
$M_* < 10^9$		8.17	8.27	5.21	–2.96	19.8	–1.18	–9.35	0.38	0.38
$M_* > 10^9$		9.89	9.85	7.19	–2.69	18.3	–0.07	–9.95	0.50	1.18

[a] For these sources, we use SFR and SSFR estimates using the same method for SFR as C15 since the MAGPHYS SFR and SSFR PDFs show two peaks. The two peaks occur because the model SFR (averaged over the last 10^8 years) will be quite different if it includes a burst (that ended nearly 10^8 years ago), compared to if the burst ended just before 10^8 years ago, even though there are only very small differences to the SEDs. Schofield et al., (*in prep.*) will explore this issue in more detail. We note that the C15 SFR estimates would be biased when the SSFR is small and the dust luminosity has a large contribution from heating by old stars (Boquien et al., 2016). This is not the case for these galaxies.

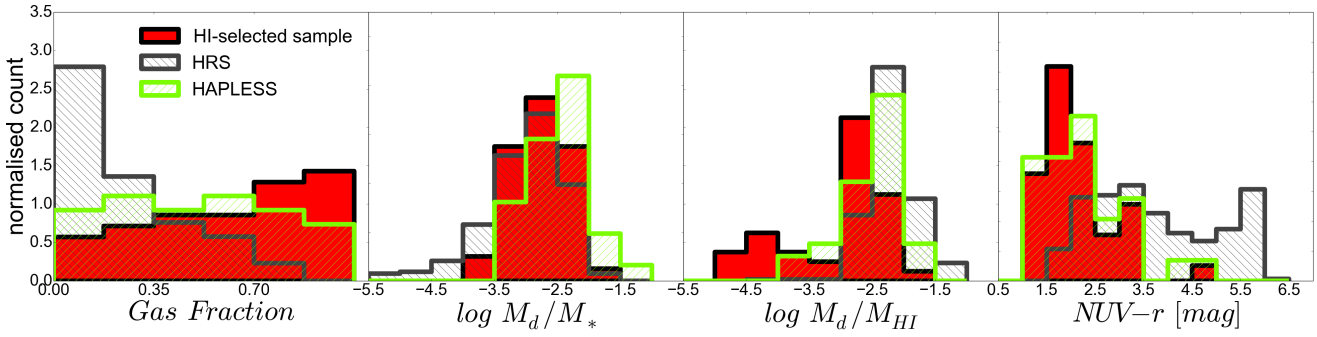

Figure 1. *From left to right:* Histogram showing the distribution of gas fraction ($\frac{M_{HI}}{M_*+M_{HI}}$), specific dust mass, dust-to-HI ratio and NUV-*r* colour (proxy for specific star formation rate) for the HIGH sample, HAPLESS and HRS.

The HIGH sample consists mainly of very blue, low surface brightness gas rich sources which have irregular or flocculent morphologies and are actively forming stars. The blue sources in our sample divide into dust rich and dust poor subsamples at $M_* \sim 10^9$ $M_\odot$ (see also Figure 2). The blue dust rich sources were already discussed in C15 and constitute around half of all dust mass selected galaxies in the local volume. In the rest of this work we will highlight the new population of blue, dust poor sources as a separate sub-sample, using a stellar mass cut of $M_* < 10^9$ $M_\odot$. We will use this criterion to split the HIGH sample into HIGH-low (for $M_* < 10^9$ $M_\odot$) and HIGH-high (for $M_* > 10^9$ $M_\odot$) throughout the rest of this work.

In Figure 2 we show the stellar, dust and HI mass scaling relations. In the left panel we find a strong correlation between dust and stellar mass for both HIGH (Spearman rank correlation coefficient r = 0.93) and HAPLESS (r = 0.81). For HRS there is a strong correlation (r = 0.88) for the Late Type Galaxies (LTGs), yet the correlation weakens significantly (r = 0.30) if the ETGs are included. Comparing the HI and stellar masses (centre panel of Figure 2), we find the strongest correlation for HIGH (r = 0.77), a weaker one for HAPLESS (r = 0.67) and the weakest for the HRS LTGs (r = 0.63). When the ETGs are included, there is no significant correlation for HRS. The HRS and the HIGH sample segregate in this plot because they intrinsically consist of galaxies in different stages of evolution (stellar mass selection favours lower gas fractions and vice versa). In the right panel of Figure 2 we find a strong correlation between the HI and dust mass for HAPLESS, the HRS and the HIGH-high sample (Spearman rank coefficient of r = 0.74 for the combined samples). However HIGH-low lies significantly below this relation and we will investigate the reasons for this in the following sections. Interestingly, The HRS ETGs now follow the same trend as the LTGs. For a given HI mass, HAPLESS and HIGH have lower dust masses on average than the HRS.

4.1 Gas richness and specific star formation rate

Figure 3 show how gas richness (M_{HI}/M_*) scales with stellar mass and NUV-*r*, which is known to be a good proxy for SSFR (e.g. Schiminovich et al., 2007). These relations have been extensively studied for HRS (Cortese et al., 2011), ALFALFA (Huang et al., 2012), Hα3 (Gavazzi et al., 2013), GASS (Catinella et al., 2013) and in earlier work (Gavazzi &Scodeggio, 1996; Boselli et al., 2001). As seen in Figure 3, the HIGH sample follows the same relations as determined for other HI selected samples, such as ALFALFA.

Some of the selection effects for the different samples are evident in the top panel. The HI selection of HIGH (and ALFALFA) selects higher M_{HI}/M_* at fixed M_* compared to the stellar mass selection of HRS. This is due both to the HI selection favouring gas rich galaxies (and *vice-versa* for stellar mass selection), and also in part to a fraction ($\sim$ 25 per cent) of the HRS sources being in the Virgo cluster. In Figure 3 we have used open symbols for HI deficient LTGs in HRS. Following Cortese et al. (2011), we consider galaxies to be HI deficient if $Def_{HI} \geqslant 0.5$ (this corresponds to galaxies with 70 per cent less hydrogen than isolated systems with the same diameter and morphological type). Next to our best fit relation for all samples combined (excluding ETGs), we have also plotted the best fit line excluding HI deficient galaxies to illustrate the effect of including HI deficient galaxies in scaling relations.

We have also added the HIPASS detection limits at $M_* = 10^{7.5}$ $M_\odot$ and $M_* = 10^8$ $M_\odot$ as black arrows to Figure 3 (top), assuming a distance equal to the average distance for HIGH-low (29.2 Mpc). The lack of sources below the dashed line at low M_* is due to this limit. However, the upper bound of the trend in Figure 3 does not suffer these selection effects. The large range of gas fractions found at a given stellar mass indicates that, although the star formation history has a well known dependence on halo mass (more massive galaxies are more evolved; e.g. Cowie et al., 1996), local factors such as environment and gas supply play an important role (e.g. De Lucia et al., 2006) and thus cause the scatter in the top panel of Figure 3. Here we clearly see that the M_{HI}/M_* vs M_* scaling relation fit depends on the sample used. The relation for HRS (or any stellar mass-selected sample) is offset to that derived for an HI-selected sample. It is also sensitive to the environment, with samples from high density regions lying below the scaling relations.

Figure 3 (bottom) shows the gas fraction is more strongly correlated with NUV-*r* colour than with M_* (r = –0.84 and r = –0.59 respectively for all samples combined). The different samples collated here (*including the HI deficient sources*) now lie on the same best fit relation (contrary to the top panel). The range in gas fraction at fixed NUV-*r* is thus significantly smaller than at fixed M_*. This can be understood by realising that the parameters on both axes scale with the cold gas content, and shows that M_{HI}/M_* is a strong driver of the specific star formation rate (either directly, or indirectly through scaling relations with the molecular gas, which is directly involved in star formation; e.g. Bigiel et al., 2011; Schruba et al., 2011; Saintonge et al., 2011; Bothwell et al., 2014). This is in line with the scatter in the main sequence of star forming galaxies (SSFR vs M_*) being driven by the gas supply (Cortese et al., 2011;

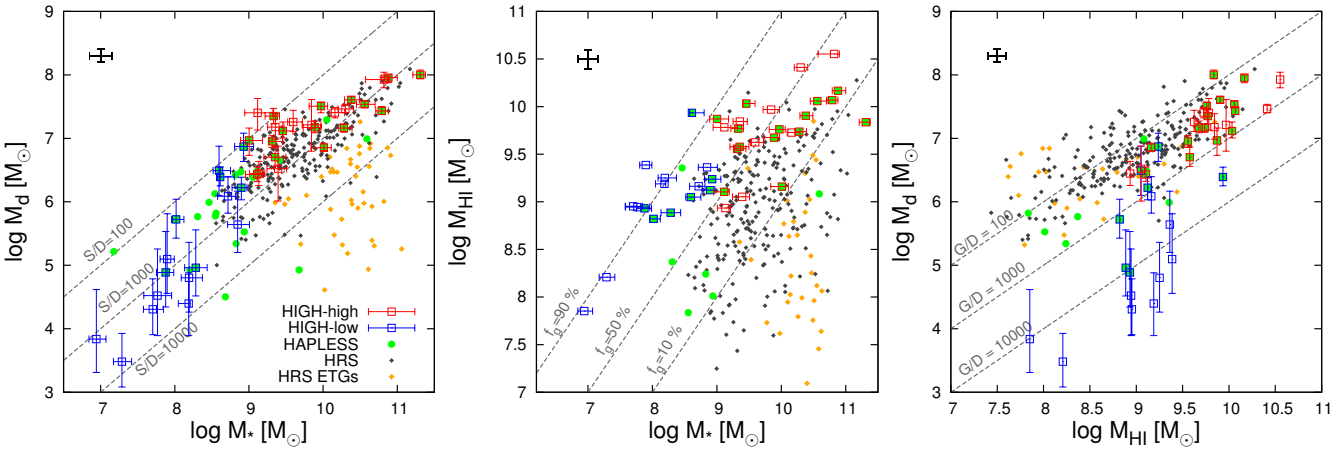

Figure 2. Scaling relations showing how the stellar, dust, and gas masses depend on each other. A representative error bar for HRS is shown in the upper-left corner. Note the selection effects towards higher dust and gas masses for the HI-selected HIGH-low (blue squares), HIGH-high (red squares) samples and the dust-selected HAPLESS sample (green circles) compared to the stellar mass selected HRS sample (grey dots). The common sources between HAPLESS and our HI-selected sub-samples are shown as green filled squares with red/blue borders. Lines of constant M_*/M_d (S/D), gas fraction (f_g) and M_{HI}/M_d (G/D) are shown in grey.

Table 2. The Spearman rank correlation coefficients (r) and lines of best fit ($y = ax + b$, where a is the slope and b is the intercept) for the significant correlations in the form of a powerlaw. The best fitting relations were determined using a BCES linear regression method (Akritas &Bershady, 1996) using the HIGH, HAPLESS and HRS samples combined. For HRS, only late type galaxies are included (both HI deficient and HI normal). The first two columns specify the x and y parameters, the last columns specify whether HIGH-low is offset and whether the derived relation is dependent on the selection used. We caution the use of relations which are strongly dependent on the selection criterea. HIGH-low is not included in the combined sample if it is offset (lower dust mass) compared to the other samples.

y	x	r	Slope	Intercept	HIGH-low offset	strong selection dependence
$\log M_{HI}/M_*$	$\log M_*$	-0.59	-0.69 ± 0.05	6.02 ± 0.47		✓
$\log M_{HI}/M_*$	NUV-*r*	-0.84	-0.65 ± 0.03	1.30 ± 0.09		
$\log M_d/M_*$	$\log M_*$	-0.44	-0.26 ± 0.03	-0.44 ± 0.34	✓	✓
$\log M_d/M_*$	log SSFR	0.72	0.51 ± 0.03	2.30 ± 0.30	✓	
$\log M_d/M_*$	NUV-*r*	-0.77	-0.33 ± 0.02	-1.92 ± 0.06	✓	
$\log M_d/M_*$	$\log M_{HI}/M_*$	0.87	0.47 ± 0.02	-2.59 ± 0.02	✓	
$\log M_d/M_{HI}$	$\log M_*$	0.47	0.32 ± 0.04	-5.33 ± 0.37	✓	✓
$\log M_d/M_{HI}$	NUV-*r*	0.66	0.28 ± 0.02	-3.06 ± 0.07	✓	
$\log M_d/M_{HI}$	$\log M_{HI}/M_*$	-0.86	-0.52 ± 0.02	-2.57 ± 0.02	✓	
$\log SFR/M_d$	$\log M_{HI}/M_*$	0.37	0.25 ± 0.03	-7.19 ± 0.03	✓	
$\log SFR/M_{HI}$	$\log M_{HI}/M_*$	-0.53	-0.29 ± 0.03	-9.80 ± 0.02		
$\log SFR/M_{HI}$	$\log \Sigma_*$	0.58	0.50 ± 0.06	-10.28 ± 0.07		

Catinella et al., 2010; Huang et al., 2012; Santini et al., 2014). We have checked this is the case for our samples by colour-coding data by HI mass in the relation between SSFR and M_*.

4.2 Specific Dust scaling relations

Cortese et al. (2012a) and Bourne et al. (2012) have studied specific dust (M_d/M_*) scaling relations for HRS and for H-ATLAS stacks on optically selected sources respectively. They found a strong anti-correlation between M_d/M_* with NUV-*r* colour and a weaker anti-correlation with stellar mass, similar to the scaling relations for M_{HI}/M_* in the previous section (see also: da Cunha et al., 2010; Smith et al., 2012; Rowlands et al., 2014a). Viaene et al. (2014) also note a similar trend for regions inside M31, indicating that the driving processes for these scaling relations (most likely star formation) are local processes. Cortese et al. (2012a) also found a strong correlation of M_d/M_* with gas fraction. Figure 4 shows the specific dust scaling relations for the different samples. We find the scaling relations for HRS, HAPLESS and HIGH-high are consistent with those in Cortese et al. (2012a) and Bourne et al. (2012).

For HIGH-low however, we find that the sources lie significantly below the trends for the other samples in each of the scaling relations in Figure 4. *The benchmark dust scaling relations identified by Cortese et al. (2012a) and Bourne et al. (2012)*[6] *based on optically selected samples, do not hold for gas rich, low* M_*

[6] Note that the H-ATLAS stacks only extend down to $M_* = 10^{8.5}\ M_\odot$ so the drop in M_d/M_* for our low stellar mass sources does not contradict the statistically significant trend for the stacks.

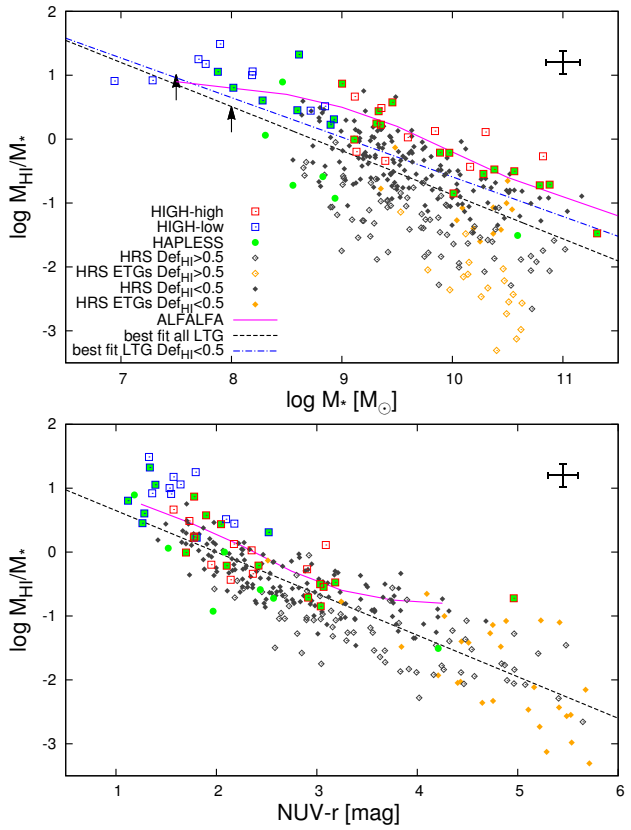

Figure 3. Trends with M_{HI}/M_* and SSFR. Symbols are as in Figure 2, with open symbols for HI deficient ($Def_{HI} \geqslant 0.5$) LTGs in HRS and filled symbols for HI normal HRS LTGs. The best fit power law relationship for the combined samples (excluding ETGs) is shown as a black dashed line, and the best relation also excluding HI deficient HRS galaxies as a blue dash-dot line. *Top:* M_{HI}/M_* against stellar mass. The ALFALFA relation (Huang et al., 2012) is shown in magenta. The HIPASS detection limits at $M_* = 10^{7.5}\,M_\odot$ and $M_* = 10^{8}\,M_\odot$ are shown as black arrows. *Bottom:* M_{HI}/M_* against NUV-*r* colour (proxy for SSFR). This strong correlation is applicable to all samples and thus is a very useful scaling relation.

(unevolved) sources. We note that a larger sample is necessary to determine the appropriate relationship for these low M_* sources.

For the HRS, HAPLESS and HIGH-high samples, we find that M_d/M_* correlates most strongly with M_{HI}/M_* ($r = 0.87$), followed by SSFR ($r = 0.72$) and then stellar mass ($r = -0.44$). For the scaling relations with stellar mass in Figure 4 (left), we find an offset towards higher M_d/M_* for the HIGH-high and HAPLESS samples compared to HRS (similar to Figure 3). This offset is absent in the scaling relations with SSFR and M_{HI}/M_*, which appear to be the more fundamental parameters driving the specific dust mass.

In the centre panel of Figure 4 we have plotted M_d/M_* against SSFR, and have added the sample of high-redshift SubMillimetre Galaxies (SMGs) from Rowlands et al. (2014a), which were also fitted with MAGPHYS. These galaxies are forming stars at a remarkably high rate and lie on a relation that extends the trend for HIGH-high, HAPLESS and the HRS (the best fit relation was not fitted to the SMGs). The correlation of M_d/M_* with SSFR holds over 5 orders of magnitude. This is consistent with the general idea that dust likely traces the molecular ISM where star-formation occurs (Dunne et al., 2000; Cortese et al., 2012a; Smith et al., 2012; Rowlands et al., 2014a). Despite the large differences in galaxy properties among the HIGH-high, HAPLESS and HRS samples, there is no evidence that they are forming stars in a fundamentally different way, they just have more or less star formation occurring as a result of their varying gas fractions. Figure 4 (centre) also shows that, for all but the most immature sources in HIGH-low, dust mass is a reasonable indicator of SFR across a very wide range of M_* and galaxy type.

Since M_{HI}/M_* is a proxy for how far a galaxy is through its evolution, the correlation seen in the right panel of Figure 4 implies that M_d/M_* depends on the evolutionary state. As galaxies evolve, they move from high to low M_{HI}/M_* and (for HIGH-high, the HRS and HAPLESS) M_d/M_* decreases. The unevolved sources in HIGH-low clearly lie below the relation for the other samples and imply a rising M_d/M_* at the earliest stages of evolution ($M_{HI}/M_* > 10^{0.5}$). *At high gas fractions, dust is not a good tracer of the the HI content*. These galaxies must be increasing their dust content at a faster fractional rate than their stellar content. The combined samples have allowed us to find a peak in the specific dust mass (M_d/M_*) in the local Universe occuring at a gas fraction of ~ 75 per cent and a stellar mass of $M_* = 10^{8.5}$. HIGH-low is the first sample of galaxies to be identified as preceding this peak M_d/M_* in an evolutionary sequence.

4.3 Dust enrichment relations

We next look at the dust content of the ISM as a function of stellar mass, NUV-*r* colour and M_{HI}/M_* (Figure 5), where we find different scaling relations for HIGH-low. For HIGH-high, HAPLESS and the HRS there is a weak but significant correlation between M_d/M_{HI} and M_* ($r = 0.47$). For HIGH-low, however, we find a steeper slope (Table 2) and a significantly smaller M_d/M_{HI} than expected from extrapolating the relation for the other samples. We find tighter scaling relations with NUV-*r* colour ($r = 0.66$) and gas richness ($r = -0.86$) for HIGH-high, HAPLESS and the HRS and again an offset towards lower dust enrichment for HIGH-low. Note again the offset between the HIGH-high/HAPLESS samples and the HRS for the stellar mass scaling relations (cf. Figures 3 & 4). Once again HI deficient galaxies are offset when M_d/M_{HI} is plotted against M_*, yet this offset disappears for the more fundamental relations of M_d/M_{HI} with NUV-*r* colour and M_{HI}/M_*. The offset between the samples is once again caused by differences in gas fractions at fixed stellar mass. Our interpretation of these dust enrichment relations is as follows:

Gas is continuously converted into stars and dust is produced at the endpoints of stellar evolution (supernovae and AGB stars). Yet at the same time dust is destroyed by shocks and also via astration as the ISM at the ambient dust-to-gas ratio forms the next generation of stars. For HIGH-high, HAPLESS and the HRS we have found positive correlations of the dust-to-gas ratio with stellar mass and NUV-*r* colour, together with a negative correlation with the gas richness, showing that M_d/M_{HI} increases monotonically as galaxies move through their evolution. This implies that the dust destruction budget is not dominated by dust destruction through shocks or sputtering. If it was, we would observe a decrease in the dust-to-gas ratio as galaxies evolve. Some of the ETGs in HRS may be an exception to this. These ETGs are bright X-ray sources and some have AGN in their centres. The hot gas in these sources erodes and breaks up the dust grains (sputtering), significantly reducing the dust mass and resulting in the outliers towards low M_d/M_{HI} for HRS in Figure 5.

In Figure 6, we follow C15 in plotting M_d/M_{bary} mass ratio

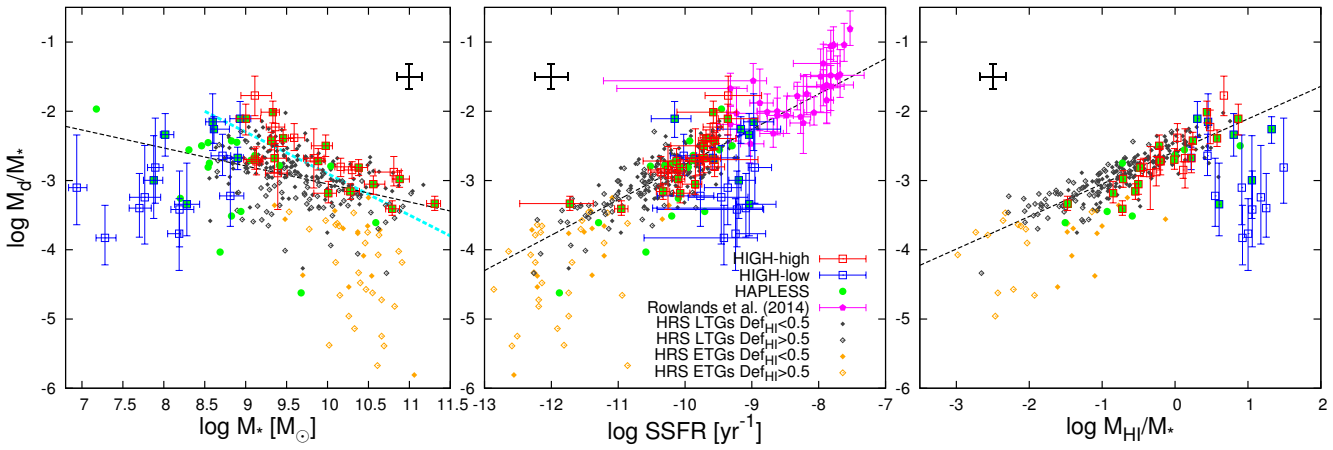

Figure 4. M_d/M_* scaling relations for for the two HI-selected sub-samples, HRS and HAPLESS. *From left to right:* Scaling relations with stellar mass, SSFR and M_{HI}/M_*. Correlations are found for each of the scaling relations for the high stellar mass HI-selected sample, HAPLESS and the HRS and the line of best fit for these 'evolved' samples combined is shown as a black dashed line. The relation from Bourne et al. (2012) for blue optically selected galaxies is given as a cyan dashed line. The ETGs are not included in our best fit relations. The symbols are as in Figure 3.

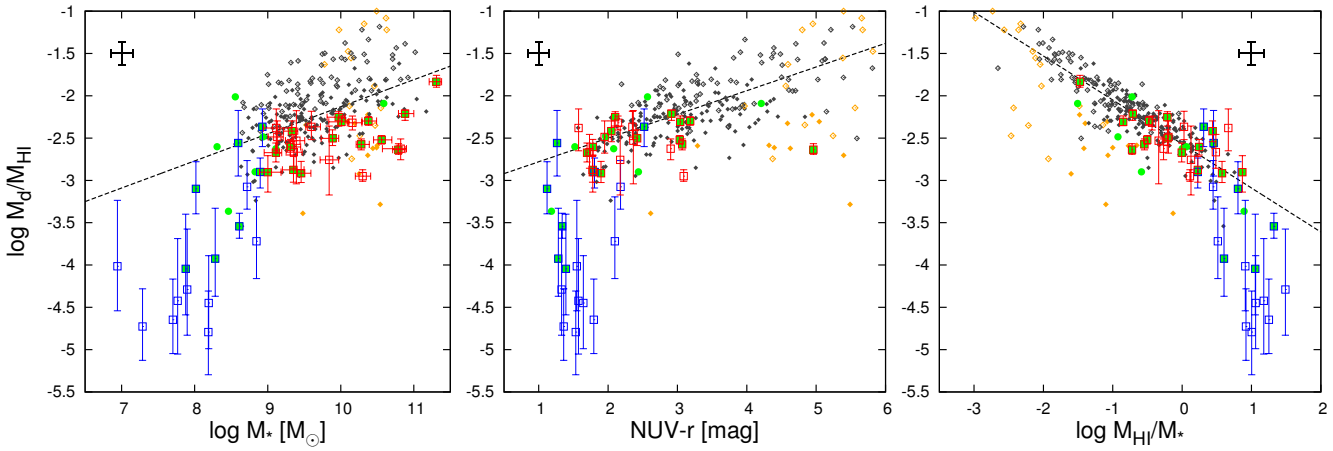

Figure 5. Dust enrichment relations for HRS, HAPLESS and HIGH. *From left to right:* Scaling relations with stellar mass, NUV-*r* colour (proxy for SSFR) and M_{HI}/M_*. The line of best fit for the combined 'evolved' samples (HIGH-high, HAPLESS and HRS) is shown as a black dashed line. The HIGH-low sample lies significantly below the trend for the other samples and has a steeper slope. The symbols are as in Figure 3.

vs gas fraction f_g (their Figure 21) where we define the baryon mass as $M_{bary} = M_{HI} + M_*$ and $f_g = M_{HI}/(M_{HI} + M_*)$. Note that we do not have CO data for HIGH and HAPLESS so we cannot measure the molecular gas mass present in these galaxies. We also follow C15 in comparing the observations with a simple, closed box chemical evolution track[7] showing the expected change in M_d/M_{bary} with gas fraction for a Milky Way type star formation history (Yin et al., 2009). The track (solid line; same as C15) shows the evolution of a galaxy as it evolves from gas rich to gas poor, with gas consumed by star formation.

Combining HIGH with HAPLESS and HRS allows us to sample a wider range of f_g. As in C15, we see M_d/M_{bary} first rises steeply, then levels off and then drops again as galaxies evolve from high to low gas fractions. This supports the idea of the dust content being built up as galaxies move through the early stages of their evolution (gas fraction > 0.8). The dust content then plateaus as dust destruction through astration balances the dust production. Note that while the position of a galaxy in Figure 6 does not depend on its total mass, since both axes are ratios, when sampling at the current epoch we find that the highest M_* galaxies are at the right of the plot and the lowest M_* are at the left, because massive galaxies go through their evolution faster. Including the HIGH sample provides crucial information at the highest gas fractions compared to the initial study in C15.

Of course, galaxies are far more complex than our simple model, with inflows and outflows and dust destruction expected to be important factors. A more detailed study of the build up of dust at high gas fractions will be presented in paper II (De Vis et al., *in prep.*), and trends with metallicity will also be studied (high gas fraction sources have significantly lower metallicities than low gas

[7] Further details on the model are presented in Rowlands et al. (2014b; see also Morgan &Edmunds, 2003)

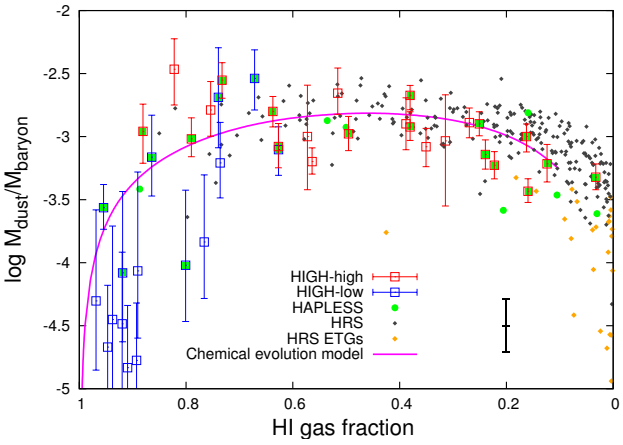

Figure 6. M_d/M_{bary} against gas fraction (without molecular hydrogen) reveals the evolution of dust. As galaxies evolve, the dust content first increases (high gas fraction), then reaches its peak for a gas fraction of ~ 0.5 and afterwards decreases as dust is consumed together with the gas (low gas fraction tail). A chemical evolution model (C15) is also shown.

fraction sources). However, even with the simplistic approach in C15, *the model is still able to match the observed overall shape of the build-up and destruction of dust as a galaxy evolves.*

5 THE EVOLUTION OF STAR FORMATION EFFICIENCY

In Figure 7, we look at two measures of the star formation efficiency of the galaxies as a function of their gas fraction (or evolutionary status). In the top panel we consider SFR/M_d, while in the bottom two panels we show SFR/M_{HI}. Our interpretation of these quantities is that SFR/M_d is a proxy for the molecular star formation efficiency to the extent that dust is a good tracer of molecular gas in galaxies (Dunne et al., 2000; Planck Collaboration et al., 2011; Corbelli et al., 2012; Rowlands et al., 2014a; Scoville et al., 2014; Santini et al., 2014). As molecular gas is directly involved in star formation (e.g. Bigiel et al. (2008); Schruba et al. (2011)), SFR/M_{H2} (aka SFR/M_d) is an indicator of the efficiency with which gas is converted to stars inside the radius at which molecular clouds are present in the galaxy.[8]

On the other hand, atomic hydrogen does not directly form stars, it must first make a transition to molecular form. SFR/M_{HI} is therefore not a true star formation efficiency but rather an indication how effectively the HI is able to turn into molecular form and subsequently form stars. With this distinction in mind, we now turn to the trends shown in Figure 7. Taken at face value, and assuming a canonical value for M_d/M_{H2} of 0.007 (Draine et al., 2007; see also Corbelli et al., 2012), the top panel of Fig 7 shows that the star formation efficiency in galaxies declines as they evolve, with the relationship in Table 2 indicating a rise in the molecular gas depletion timescale (τ_{H2}) from 1.7 Gyr to 4 Gyr over a range in gas fraction from 80-10 per cent. The HIGH-low sample lies well above this relationship indicating either a much shorter molecular gas depletion time (average of 140 Myr), or a much lower M_d/M_{H2} ratio (by a factor ~ 10). Resolving this issue would require resolved CO + HI maps for these sources.

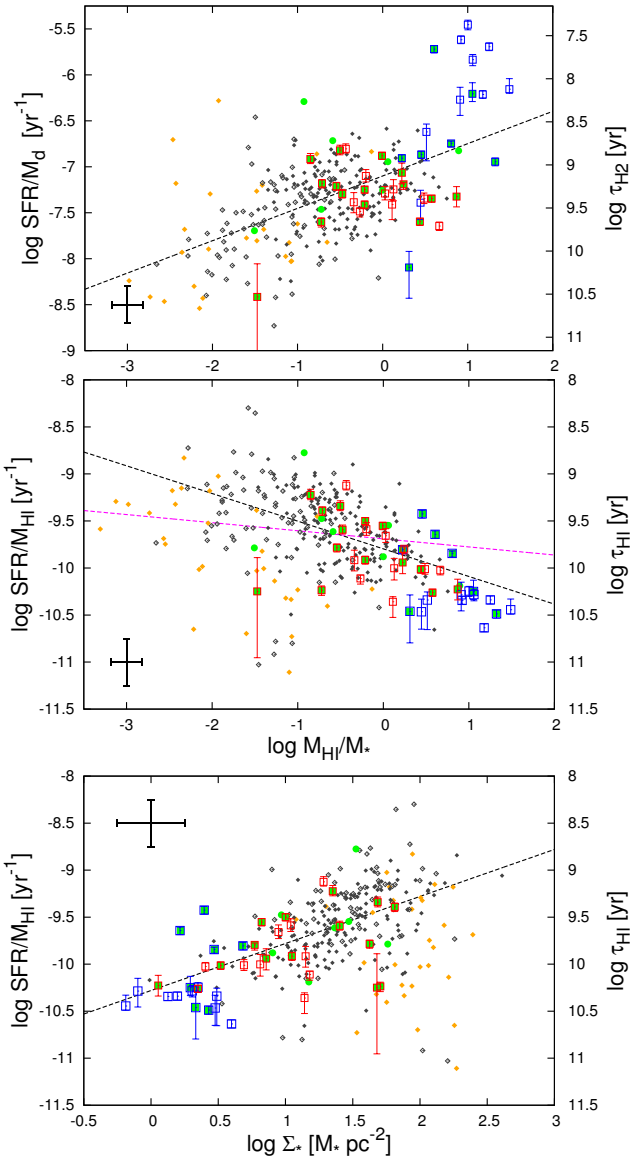

Figure 7. *Top:* SFR/M_d against M_{HI}/M_* showing a slow decline of SFR/M_d as galaxies evolve. HIGH-low is significantly offset towards higher SFR/M_d. The right axis shows the molecular gas depletion timescale using M_d as a proxy. *Centre:* SFR/M_{HI} against M_{HI}/M_*. There is a clear evolution towards higher SFR/M_{HI} for more evolved sources (best-fit line including all samples is shown in dashed black). The correlation resulting from a typical HI error of 0.1 dex has been determined using MC simulations (dashed magenta). *Bottom:* Star formation rate per HI mass (SFR/M_{HI}) against stellar mass surface density Σ_*.

Studies of the other main molecular gas tracer (CO) in local galaxies selected over a range of stellar mass from $8.5 < \mathrm{Log}\, M_* < 11.5$, find a similar result; that the star formation efficiency increases (or the gas depletion time decreases) as the stellar mass decreases and as SSFR increases (Saintonge et al., 2011; Bothwell et al., 2014; Boselli et al., 2014a).[9] These studies find a range of

[8] For a true measure of the efficiency of converting dense gas into stars within star forming regions, it is necessary to choose a high density molecular tracer (e.g. HCN) Gao &Solomon, 2004; Papadopoulos et al., 2012.

[9] Earlier studies of the molecular gas depletion times in local spiral galax-

τ_{H2} from 100 Myr – 5 Gyr over the same range of stellar mass as sampled here although our study contains three samples selected in very different ways (dust, gas and stellar content)[10].

In the centre panel of Figure 7 we find that there is considerable evolution in SFR/M_{HI} ($r = -0.53$), such that more evolved galaxies have higher star formation per HI mass (shorter HI depletion times, τ_{HI}, assuming constant star formation rate and no resupply of gas). We must be cautious in interpreting Figure 7 (centre) as the quantity M_{HI} is present in both the x and y axes. Monte Carlo simulations were used to confirm that this relation cannot be due to biases introduced by the errors in M_{HI}. For each source in the sample, we generated an artificial HI mass so that its SFR/M_{HI} is equal to the average SFR/M_{HI} in the whole sample (the null hypothesis is that there is no evolution in SFR/M_{HI}) and then added Gaussian scatter with a standard deviation of 0.1 dex (typical M_{HI} error). This process was repeated 100 times and the resulting average trend is shown by the magenta line in Figure 7 (centre). The error on M_{HI} does introduce an artificial correlation, however, the observed slope in Figure 7 (centre) is significantly steeper and we believe this is a real effect.

The galaxies with the highest gas fractions, which were previously found to be the most actively star forming galaxies in terms of their stellar mass (SSFR) and their dust mass (SFR/M_d), are now least active with respect to their HI mass (they have the lowest SFR/M_{HI}). The HI depletion timescales range from 0.2 – 63 Gyr, with the most gas rich ($M_{HI} > M_*$) sources capable of sustaining their current star formation rates for longer than the Hubble time. Previous studies find a comparable range in the value of τ_{HI} but no trend with any of the parameters which correlate with τ_{H2} e.g. stellar mass, SSFR (Saintonge et al., 2011; Bothwell et al., 2014; Boselli et al., 2014a). Similarly, we do not find a correlation of τ_{HI} with either stellar mass or SSFR.

There is, however, a known relationship between τ_{HI} and stellar mass surface density (Σ_*) *within* galaxies. The THINGS survey (Walter et al., 2008; Leroy et al., 2008) found SFR/M_{HI} to be a strong and almost linear function of stellar mass surface density in the outer regions of spirals and in dwarfs, where the ISM is dominated by HI. Within the inner regions of spiral galaxies, the higher stellar mass surface density produces a higher hydrostatic pressure in the ISM (Elmegreen, 1989; Wong &Blitz, 2002) favouring the conversion of HI to H_2 and results in a molecular dominated region where the star formation efficiency (τ_{H2}) is constant. We find a correlation ($r = 0.58$) between the global τ_{HI} and stellar mass surface density in the bottom panel of Figure 7. This is the first time that such a relationship has been reported for global values *between* galaxies.

We can use Figure 7 (bottom) to interpret the top two panels as being the result of an increasing efficiency of conversion of $H_I \rightarrow H_2$ as galaxies become more dominated by their stellar mass. As galaxies build up their stellar mass and increase in Σ_* they create the conditions for H_2 formation across a wider area; and their HI reservoirs are depleted due to conversion to H_2 and thence to stars. As galaxies become very dominated by stars and have large bulges, they can be H_2 dominated over large areas and their HI reservoirs will be relegated to the outskirts of the galaxy. In very evolved galaxies (e.g. ETGs) the presence of gas and star formation will be more strongly correlated with recent interactions or environmental effects (Davis et al., 2011; Kaviraj et al., 2012; 2013; Davies et al., 2015). This may explain the very large scatter in τ_{HI} for the lowest gas fraction galaxies.

This general picture is not strongly dependent on an assumption of a constant dust/H_2 ratio, that ratio would need to vary by several orders of magnitude to invalidate this interpretation. Detailed observations of resolved CO, HI and dust would be required to further elaborate on this.

6 DUST HEATING IN THE DIFFUSE ISM

Dust in the diffuse ISM is heated by the interstellar radiation field (ISRF), which has contributions from both old and young stellar populations. Dust in birth clouds experiences more intense and harsh radiation fields in the photo-dissociation regions (PDRs). To account for this MAGPHYS has a parameter, f_μ, which represents the fraction of the total dust luminosity arising in the diffuse ISM. The majority of the dust mass resides in a cold ($10 < T < 30$ K) diffuse dust component, whereas in most actively star forming galaxies a large fraction of the dust luminosity is due to a warm ($30 < T < 60$ K) dust component arising in birth clouds (futher details of the MAGPHYS components are found in Section 2.4).

In a typical galaxy in the local universe much of the stellar mass is in low mass stars, yet the small fraction of massive, short-lived stars radiate much more strongly at UV wavelengths. This UV radiation is highly susceptible to absorption by dust and the high energy UV photons can cause much of the dust heating (e.g. Draine et al., 2007) even though they only make up a very small fraction of the photons in the ISRF. In birth clouds the UV photons from young stars dominate the dust heating, but even in the diffuse ISM the PAHs, small grains (stochastically heated and emitting at MIR) and warm dust components are still mostly heated by UV photons that leak from the birth clouds and form part of the diffuse ISRF (Devereux &Young, 1990; Kennicutt, 1998; Calzetti et al., 2005; 2007; Boquien et al., 2010; Bendo et al., 2012; Kirkpatrick et al., 2014). Many literature works have studied the sources of dust heating for the bulk of the dust mass in the diffuse ISM, and found that both the young stars in star forming regions and the diffuse evolved populations heat the diffuse dust (Bendo et al., 2010; Boselli et al., 2010b; 2012; Foyle et al., 2013; Ciesla et al., 2014; Cortese et al., 2014; Kirkpatrick et al., 2014; Draine et al., 2014; Bendo et al., 2015, C15). In this section we will study which parameters drive change in f_μ and cold dust temperature and investigate which source of dust heating dominates in a particular galaxy for a wide range of gas fraction.

Figure 8 shows an anti-correlation of f_μ with SSFR for all the samples. In order to probe to the highest SSFR, we have included the high redshift SMGs from Rowlands et al. (2014a). As expected, for most galaxies the fraction of the total dust luminosity originating in the birth-clouds ($1 - f_\mu$) is proportional to the star forming activity of the galaxy. This would be the case if a reasonable fraction of the energy in the birth clouds was being absorbed locally and re-radiated by dust (i.e. at least moderate A_{FUV}). Outliers can occur if the UV attenuation in the birth clouds is very low, allowing most of the UV energy to escape and heat the dust in the diffuse dust component. We indeed find that the outliers towards high f_μ in Figure 8 are all amongst the least attenuated sources in the sample ($A_{FUV} < 0.35$; see next section). On the other hand, outliers can also occur if a considerable fraction of the dust is heated by AGN

ies found a constant τ_{H2} of ~ 2 Gyr (e.g. Bigiel et al., 2008; Leroy et al., 2008), however these studies probed a much smaller range of intrinsic stellar mass or gas fraction and so are not thought to contradict the later findings of these larger studies.

[10] One of the samples (HRS) is the same as that used by Boselli et al. (2014a) though we are using dust as a tracer of H_2 rather than CO.

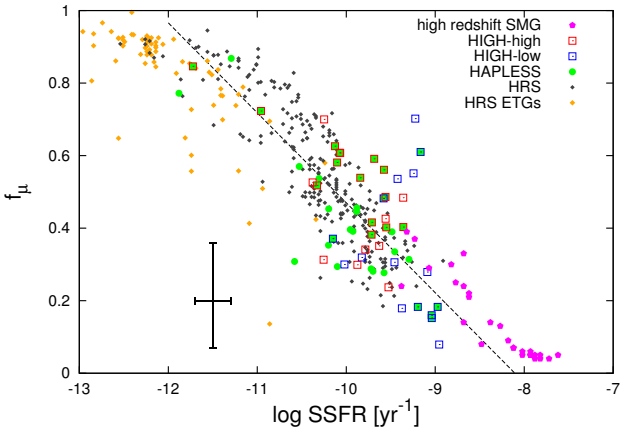

Figure 8. Influence of SSFR on the fraction of the total luminosity that originates in the diffuse ISM (f_μ). Less actively star forming galaxies have a larger fraction of their dust luminosity originating in the diffuse ISM. The line of best fit for combined HAPLESS, HiGH and SMG (Rowlands et al., 2014a) samples is shown as a dashed black line.

activity or the hot X-ray halo that is often present in ETGs, as these sources of heating are not included in the MAGPHYS prescription. All the outliers towards low f_μ are ETGs and the strongest outliers are known bright X-ray sources.

Both the young stars (traced by the SFR) and the old stars (traced by M_*) play a role in heating the diffuse dust. Figure 9 provides us with a graphical way to understand the contributions from the old and young stellar populations to the total and cold dust heating. We have plotted M_*/M_d against SFR/M_d and colour-coded the data by cold dust temperature and f_μ respectively (again including the SMGs from Rowlands et al., 2014a).

Even discounting the SMGs[11], which generally lie off the main sequence of star formation, we find only a very weak correlation between SFR and M_* *after normalising by dust mass*. There is a clear trend towards higher temperatures as one goes to higher M_*/M_d or SFR/M_d. For a fixed M_*/M_d, we find the spread in temperatures largely follows the differences in SFR/M_d and the same when fixing SFR/M_d and varying M_*/M_d. This explains why ETGs have warm T_c, as despite having low SFR their M_*/M_d are the highest, and so their old stellar radiation fields are intense enough to heat the diffuse dust to warmer temperatures. At $SFR/M_d > 10^{-6.5} yr^{-1}$, there no longer seems to be any dependence of T_c on M_*/M_d, probably because the dust heating is completely dominated by the young stellar population for these galaxies and the old stellar population has little effect. For galaxies with $SFR/M_d < 10^{-6.5} yr^{-1}$, both the young and old stellar populations heat the cold dust component, with some dominated by one and some by the other.

Figure 9(bottom) shows that the direction of increasing f_μ (also direction of increasing SSFR) is nearly orthogonal to the direction of increasing T_c. This means that the cold dust temperature is more or less independent of the fraction of the total dust luminosity originating in the diffuse ISM (i.e. T_c is not affected by the SSFR). However the fraction of the dust luminosity originating from heating by old stars is inversely proportional to SSFR (Boquien et al., 2016). Galaxies in the upper left quadrant of Figure 9

[11] Including the SMGs leads to an even weaker correlation.

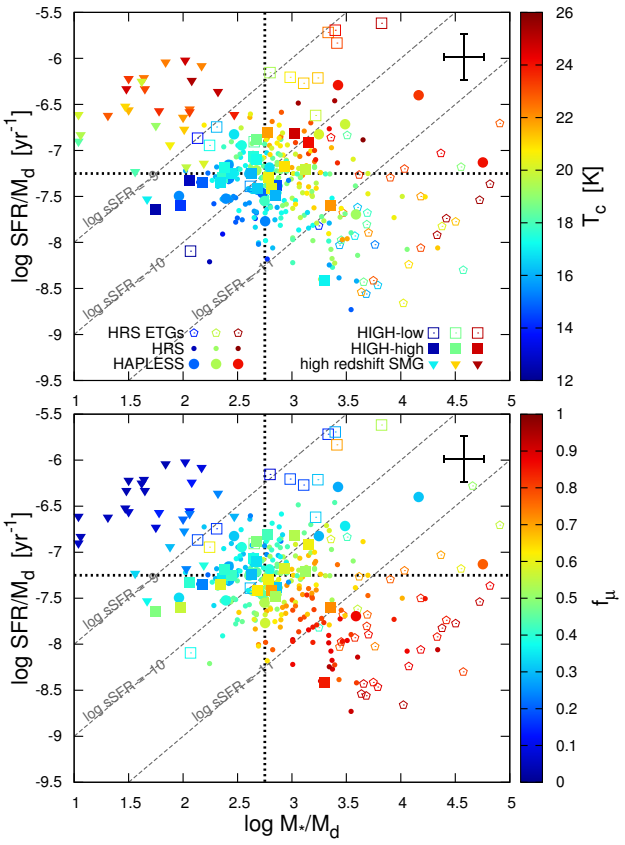

Figure 9. M_*/M_d against SFR/M_d, colour-coded by cold dust temperature T_c (*top*) and the fractional contribution of diffuse dust to the total dust luminosity, f_μ (*bottom*) in order to study the sources of dust heating. These plots have been divided in 4 'heating' quadrants to highlight the differences. Lines of constant SSFR are shown in dashed gray.

have most of the dust luminosity originating in birth clouds and the dust heating is dominated by photons from young stars. Galaxies with moderate SSFR have dust emission from both birth clouds and the diffuse ISM as well as significant contributions to the heating of the diffuse dust from both young and old stars. These galaxies can be dust rich and cold (lower left quadrant) or dust poor and warmer (upper right quadrant). Finally, quiescent galaxies (lower right quadrant) have most of their dust luminosity originating in the diffuse ISM and this is heated mostly by the old stars.

7 OBSCURATION

To study how the UV obscuration depends on other galaxy properties we have plotted the MAGPHYS A_{FUV} parameter against M_{HI}/M_*, Σ_* and dust mass in Figure 10. In the left panel we find an anti-correlation ($r = -0.54$) for A_{FUV} with M_{HI}/M_*. As galaxies move through their evolution, from gas rich to gas poor (right to left on this plot) the obscuration initially increases. This makes sense as dust is continuously produced and mixed with the ISM. Note that all galaxies with $\log M_{HI}/M_* > 0.5$ approach $A_{FUV} = 0$, which corresponds to the limit of no obscuration. From Figure 5 this corresponds to $\log M_d/M_{HI} < -3$.

The sources with the highest obscuration have the highest cold dust temperatures and are on average slightly more inclined than

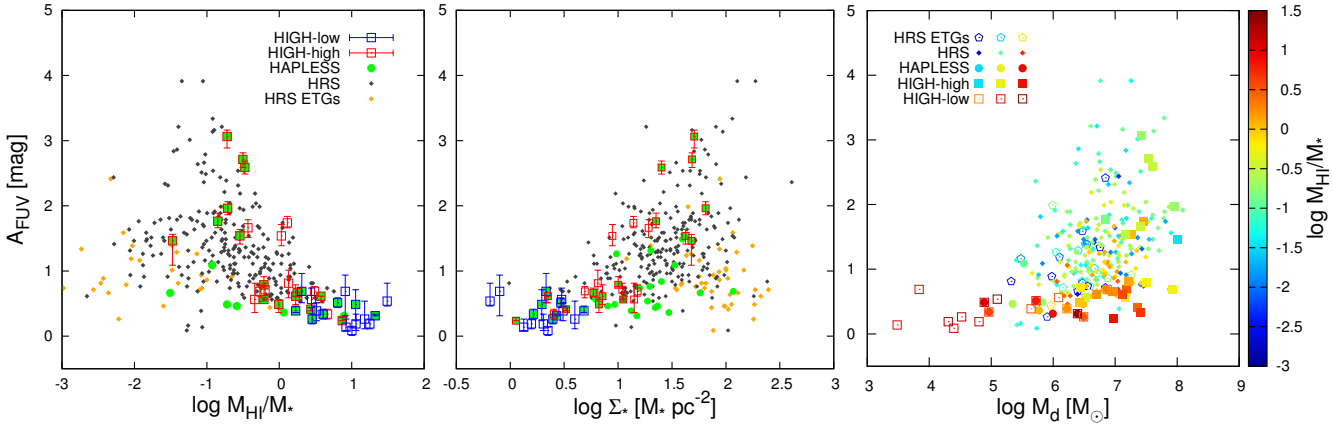

Figure 10. The variation of FUV attenuation A_{FUV} with galaxy parameters. *Left:* The obscuration increases as one moves from high to low gas fraction (i.e. from less to more evolved sources). *Centre:* Relationship between A_{FUV} and stellar mass surface density Σ_*. *Right:* For low dust masses ($M_d < 10^5 M_\odot$) there is little to no obscuration. We find a positive correlation between the obscuration and the dust mass above this value for the HAPLESS and HIGH samples. The outliers towards high obscuration at moderate dust masses are evolved sources in HRS ($\log M_{HI}/M_* < -0.6$). For all three plots there is a large amount of scatter that correspond to a wide range of obscuration for a given M_d (likely due to different dust and stellar geometries).

the less obscured galaxies at the same M_{HI}/M_*. In the latest stages of evolution, the obscuration decreases again as most of the dust mass is consumed due to astration (Figure 6) or removed.

The large scatter in A_{FUV} at lower gas fractions is at least partly due to differences in the intrinsic stellar and dust geometries and inclinations of these galaxies. Attenuation strongly depends on how much of the dust is mixed into the diffuse ISM as opposed to being distributed in a more clumpy geometry, and on other geometric differences like scale heights and scale lengths of the stellar and dust disks (Baes &Dejonghe, 2001; Bianchi, 2008; Holwerda et al., 2012; Popescu et al., 2011). Investigating whether or not the star-dust geometry is the main factor that drives this scatter is a difficult task. One potential way to do that is by including realistic recipes for dust attenuation in hydrodynamical models of galaxy evolution, and comparing the attenuation properties of simulated mock galaxies to observed data. As both cosmological hydrodynamical simulations (e.g. Vogelsberger et al., 2014; Schaye et al., 2015) and 3D dust radiative transfer techniques (Steinacker et al., 2013) have reached a level of maturity, this combination has recently become possible (e.g., Camps et al., 2016; Trayford et al., *in prep.*). Such an investigation is beyond the scope of this paper, but will be the subject of future work.

Grootes et al. (2013) found a relationship between the optical depth and stellar mass surface density Σ_* of nearby spiral galaxies. We find a similar relationship ($r = 0.53$) when we plot A_{FUV} against Σ_* in Figure 10 (centre). The increased stellar mass potential associated with higher Σ_* creates instabilities in the cold ISM, which lead to the formation of a thin dust disk (Dalcanton et al., 2004). This changes the relative geometries of dust and stars which provides a possible explanation for the changes in obscuration.

The attenuation by dust is expected to depend on the total column of dust along a photon's trajectory. We show how A_{FUV} varies with the total dust mass[12], colour coded by gas fraction, in the right panel of Figure 10. We find a positive correlation ($r = 0.38$) but the relationship is not a simple power law and there is a lot of scatter. At $M_d < 10^{5.5}$ the obscuration tends to zero, while at higher dust masses, there is a large range in obscuration and again this is likely due to different stellar and dust geometries or different extinction laws. In summary we find no clear and simple link between UV obscuration and global galaxy properties.

[12] Plotting A_{FUV} against the dust surface density (which could be argued to be a better tracer of the dust mass along a photon's path), does not change the results in any way.

8 CONCLUSIONS

We have studied the interplay of dust, gas and star formation for combined samples made up of local HI-, dust- and stellar mass selected galaxies, using MAGPHYS to determine physical properties from UV to submm photometry. The combined samples cover a wide range of gas fractions (proxy for the evolutionary state of a galaxy). Our main results are:

– We have identified a sub-sample of HI-selected sources (HIGH-low) with very high gas fractions ($f_g > 80$ per cent) and low stellar masses ($M_* < 10^9 M_\odot$). These probe the earliest stages of evolution, and have a much smaller dust content than expected from extrapolating published scaling relations for more evolved sources.

– In the earliest stages of evolution ($f_g > 80$ per cent), dust is not a good tracer of the gas content. The dust content relative to stellar mass first rises steeply with decreasing gas fraction, reaches a peak at a gas fraction of ~75 per cent (which for local galaxies is equivalent to a stellar mass of $\sim 10^{8.5}$ $M_\odot$), and then decreases together with gas fraction.

– The galaxies with the highest gas fractions are the most actively star forming galaxies relative to their stellar masses (SSFR) and relative to their H_2 content (using dust as a proxy for H_2).

– We find a trend of decreasing HI depletion time with decreasing gas fraction, such that the most gas rich galaxies have the longest τ_{HI}. We interpret this, together with the opposing behaviour of τ_{H2}, as being due to the increasing efficiency with which HI can be converted to H_2 as galaxies increase in stellar mass surface density with decreasing gas fraction.

– We confirm literature results that both old and young stellar populations play an important role in heating the diffuse dust com-

ponent, and both can be the dominant contributor in individual systems. The SSFR determines which dominates.

– The FUV obscuration of galaxies shows no clear and simple link with global galaxy properties. Galaxies start out barely obscured and increase in obscuration as they evolve until the dust mass decreases significantly in the latest stages of evolution.

The derived scaling relations for the combined samples in this work span a wider range in gas fraction than previous relations in the literature, yet admittedly have somewhat complex selection biases. Since the sample size of the stellar mass selected sample (HRS) is 8 times larger than the HI- and dust-selected samples, the scaling relations are therefore heavily weighted towards this sample. This especially affects the scaling relations with stellar mass, which show significant offsets between the differently selected samples. However using the combined sample including the high gas fraction sources, we show that the most robust scaling relations for gas and dust are those linked to NUV-*r* (SSFR) and gas fraction. These are tight relations which do not depend on sample selection or environment and are thus not affected by the complex selection criteria of the combined sample.

ACKNOWLEDGMENTS

We thank the anonymous referee for useful suggestions. The authors gratefully acknowledge Martha Haynes, Riccardo Giovanelli, and the ALFALFA team for supplying the latest ALFALFA survey data. The authors also thank Ariadna Manilla Robles, Asantha Cooray, Paul van der Werf and Michal Michalowski for helpful discussions. LD, SJM and RJI acknowledge support from the ERC in the form of the Advanced Investigator Program, COSMICISM. HLG, LD and SJM acknowledge support from the European Research Council in the form of Consolidator Grant CosmicDust. CJRC acknowledges support from the European Research Council (ERC) FP7 project DustPedia (PI Jon Davies) and the STFC Doctoral Training Grant scheme. The H-ATLAS is a project with *Herschel*, which is an ESA space observatory with science instruments provided by European-led Principal Investigator consortia and with important participation from NASA. The H-ATLAS website is http://www.h-atlas.org/. GAMA is a joint European- Australasian project based around a spectroscopic campaign using the Anglo-Australian Telescope. The GAMA input catalogue is based on data taken from the Sloan Digital Sky Survey and the UKIRT Infrared Deep Sky Survey. Complementary imaging of the GAMA regions is being obtained by a number of independent survey programs including *GALEX* MIS, VST KIDS, VISTA VIKING, WISE, *Herschel*-ATLAS, GMRT, and ASKAP, providing UV to radio coverage. GAMA is funded by the STFC (UK), the ARC (Australia), the AAO, and the participating institut The GAMA website is: http://www.gama-survey.org/. This research has made use of Astropy[13], a community-developed core Python package for Astronomy (Astropy Collaboration et al., 2013). This research has made use of TOPCAT[14] (Taylor, 2005), which was initially developed under the UK Starlink project, and has since been supported by PPARC, the VOTech project, the AstroGrid project, the AIDA project, the STFC, the GAVO project, the European Space Agency, and the GENIUS project. This research has made use of of APLpy[15], an open-source astronomical image plotting package for Python. This research has made use of NumPy[16] (Walt et al., 2011), SciPy[17], and MatPlotLib[18] (Hunter, 2007). This research has made use of the SIMBAD[19] database (Wenger et al., 2000) and the VizieR[20] catalogue access tool (Ochsenbein et al., 2000), both operated at CDS, Strasbourg, France. This research has made use of SAOImage DS9[21], developed by the Smithsonian Astrophysical Observatory with support from the Chandra X-ray Science Center (CXC), the High Energy Astrophysics Science Archive Center (HEASARC), and the JWST Mission office at the Space Telescope Science Institute (STSI). This research has made use of the NASA/IPAC Extragalactic Database (NED[22]), operated by the Jet Propulsion Laboratory, California Institute of Technology, under contract with the National Aeronautics and Space Administration.

REFERENCES

Abazajian K. N., et al., 2009, ApJS, 182, 543
Adelman-McCarthy J. K., et al., 2008, ApJS, 175, 297
Ahn C. P., et al., 2012, ApJS, 203, 21
Akritas M. G., Bershady M. A., 1996, ApJ, 470, 706
Astropy Collaboration et al., 2013, A&A, 558, A33
Baes M., Dejonghe H., 2001, MNRAS, 326, 733
Baldry I. K., et al., 2012, MNRAS, 421, 621
Barnes D. G., et al., 2001, MNRAS, 322, 486
Bendo G. J., et al., 2010, A&A, 518, L65
Bendo G. J., et al., 2012, MNRAS, 419, 1833
Bendo G. J., et al., 2015, MNRAS, 448, 135
Bertin E., Arnouts S., 1996, A&AS, 117, 393
Bianchi S., 2008, A&A, 490, 461
Bigiel F., Leroy A., Walter F., Brinks E., de Blok W. J. G., Madore B., Thornley M. D., 2008, AJ, 136, 2846
Bigiel F., et al., 2011, ApJ, 730, L13
Boquien M., et al., 2010, A&A, 518, L70
Boquien M., et al., 2016, A&A, 591, A6
Boselli A., Gavazzi G., Donas J., Scodeggio M., 2001, AJ, 121, 753
Boselli A., et al., 2010a, PASP, 122, 261
Boselli A., et al., 2010b, A&A, 518, L61
Boselli A., et al., 2012, A&A, 540, A54
Boselli A., Hughes T. M., Cortese L., Gavazzi G., Buat V., 2013, A&A, 550, A114
Boselli A., Cortese L., Boquien M., 2014a, A&A, 564, A65
Boselli A., Cortese L., Boquien M., Boissier S., Catinella B., Lagos C., Saintonge A., 2014b, A&A, 564, A66
Boselli A., Fossati M., Gavazzi G., Ciesla L., Buat V., Boissier S., Hughes T. M., 2015, A&A, 579, A102
Bothwell M. S., et al., 2014, MNRAS, 445, 2599
Bourne N., et al., 2012, MNRAS, 421, 3027
Bourne N., et al., 2013, MNRAS, 436, 479
Bourne N., et al., 2016, preprint, (arXiv:1606.09254)
Calzetti D., et al., 2005, ApJ, 633, 871
Calzetti D., et al., 2007, ApJ, 666, 870
Camps P., Trayford J. W., Baes M., Theuns T., Schaller M., Schaye J., 2016, MNRAS, 462, 1057
Catinella B., et al., 2010, MNRAS, 403, 683
Catinella B., et al., 2013, MNRAS, 436, 34

[13] http://www.astropy.org/
[14] http://www.star.bris.ac.uk/ mbt/topcat/
[15] http://aplpy.github.io/
[16] http://www.numpy.org/
[17] http://www.scipy.org/
[18] http://matplotlib.org/
[19] http://simbad.u-strasbg.fr/simbad/
[20] http://vizier.u-strasbg.fr/viz-bin/VizieR
[21] http://ds9.si.edu/site/Home.html
[22] http://ned.ipac.caltech.edu/

Ciesla L., et al., 2014, A&A, 565, A128
Clark C. J. R., et al., 2015, MNRAS, 452, 397
Cluver M. E., et al., 2014, ApJ, 782, 90
Corbelli E., et al., 2012, A&A, 542, A32
Cortese L., Catinella B., Boissier S., Boselli A., Heinis S., 2011, MNRAS, 415, 1797
Cortese L., et al., 2012a, A&A, 540, A52
Cortese L., et al., 2012b, A&A, 544, A101
Cortese L., et al., 2014, MNRAS, 440, 942
Cowie L. L., Songaila A., Hu E. M., Cohen J. G., 1996, AJ, 112, 839
Dalcanton J. J., Yoachim P., Bernstein R. A., 2004, ApJ, 608, 189
Davies L. J. M., et al., 2015, MNRAS, 452, 616
Davis T. A., et al., 2011, MNRAS, 417, 882
De Lucia G., Springel V., White S. D. M., Croton D., Kauffmann G., 2006, MNRAS, 366, 499
Devereux N. A., Young J. S., 1990, ApJ, 350, L25
Devereux N. A., Young J. S., Eales S. A., 1990, in Massive Stars in Starbursts. p. 12
Draine B. T., et al., 2007, ApJ, 663, 866
Draine B. T., et al., 2014, ApJ, 780, 172
Driver S. P., Allen P. D., Liske J., Graham A. W., 2007, ApJ, 657, L85
Driver S. P., et al., 2009, Astronomy and Geophysics, 50, 050000
Driver S. P., et al., 2011, MNRAS, 413, 971
Driver S. P., et al., 2016, MNRAS, 455, 3911
Dunne L., Eales S. A., 2001, MNRAS, 327, 697
Dunne L., Eales S., Edmunds M., Ivison R., Alexander P., Clements D. L., 2000, MNRAS, 315, 115
Dunne L., et al., 2011, MNRAS, 417, 1510
Eales S., et al., 2010, PASP, 122, 499
Elmegreen B. G., 1989, ApJ, 338, 178
Fixsen D. J., Cheng E. S., Gales J. M., Mather J. C., Shafer R. A., Wright E. L., 1996, ApJ, 473, 576
Foyle K., et al., 2013, MNRAS, 432, 2182
Gao Y., Solomon P. M., 2004, ApJ, 606, 271
Gavazzi G., Scodeggio M., 1996, A&A, 312, L29
Gavazzi G., Fumagalli M., Fossati M., Galardo V., Grossetti F., Boselli A., Giovanelli R., Haynes M. P., 2013, A&A, 553, A89
Giovanelli R., et al., 2005, AJ, 130, 2598
Griffin M. J., et al., 2010, A&A, 518, L3
Grootes M. W., et al., 2013, ApJ, 766, 59
Haynes M. P., et al., 2011, AJ, 142, 170
Holland W. S., et al., 1999, MNRAS, 303, 659
Holwerda B. W., et al., 2012, A&A, 541, L5
Hopkins A. M., et al., 2013, MNRAS, 430, 2047
Huang S., Haynes M. P., Giovanelli R., Brinchmann J., 2012, ApJ, 756, 113
Hunter J. D., 2007, Computing In Science & Engineering, 9, 90
Irwin M., 2010, "UKIRT Newsletter", 26, 14
Issa M. R., MacLaren I., Wolfendale A. W., 1990, A&A, 236, 237
James A., Dunne L., Eales S., Edmunds M. G., 2002, MNRAS, 335, 753
Kaviraj S., et al., 2012, MNRAS, 423, 49
Kaviraj S., et al., 2013, MNRAS, 435, 1463
Kennicutt Jr. R. C., 1998, ApJ, 498, 541
Kessler M. F., et al., 1996, A&A, 315, L27
Kirkpatrick A., et al., 2014, ApJ, 789, 130
Kreysa E., et al., 1998, in Phillips T. G., ed., Society of Photo-Optical Instrumentation Engineers (SPIE) Conference Series Vol. 3357, Advanced Technology MMW, Radio, and Terahertz Telescopes. pp 319–325
Kreysa E., et al., 2003, in Phillips T. G., Zmuidzinas J., eds, Society of Photo-Optical Instrumentation Engineers (SPIE) Conference Series Vol. 4855, Millimeter and Submillimeter Detectors for Astronomy. pp 41–48, doi:10.1117/12.459176
Leroy A. K., Walter F., Brinks E., Bigiel F., de Blok W. J. G., Madore B., Thornley M. D., 2008, AJ, 136, 2782
Lisenfeld U., Ferrara A., 1998, ApJ, 496, 145
Lisenfeld U., et al., 2007, A&A, 462, 507
Liske J., et al., 2015, MNRAS, 452, 2087
Meyer M. J., et al., 2004, MNRAS, 350, 1195
Morgan H. L., Edmunds M. G., 2003, MNRAS, 343, 427
Morrissey P., et al., 2007, ApJS, 173, 682
Neugebauer G., et al., 1984, ApJ, 278, L1
Ochsenbein F., Bauer P., Marcout J., 2000, A&AS, 143, 23
Papadopoulos P. P., van der Werf P. P., Xilouris E. M., Isaak K. G., Gao Y., Mühle S., 2012, MNRAS, 426, 2601
Pilbratt G. L., et al., 2010, A&A, 518, L1
Planck Collaboration et al., 2011, A&A, 536, A19
Poglitsch A., et al., 2010, A&A, 518, L2
Popescu C. C., Tuffs R. J., Dopita M. A., Fischera J., Kylafis N. D., Madore B. F., 2011, A&A, 527, A109
Popping A., Braun R., 2011, A&A, 528, A28
Riess A. G., et al., 2011, ApJ, 730, 119
Roussel H., 2013, PASP, 125, 1126
Rowlands K., et al., 2014a, MNRAS, 441, 1017
Rowlands K., Gomez H. L., Dunne L., Aragón-Salamanca A., Dye S., Maddox S., da Cunha E., Werf P. v. d., 2014b, MNRAS, 441, 1040
Saintonge A., et al., 2011, MNRAS, 415, 32
Sanders D. B., Scoville N. Z., Soifer B. T., 1991, ApJ, 370, 158
Sanders D. B., Mazzarella J. M., Kim D.-C., Surace J. A., Soifer B. T., 2003, AJ, 126, 1607
Sandstrom K. M., et al., 2013, ApJ, 777, 5
Santini P., et al., 2014, A&A, 562, A30
Schaye J., et al., 2015, MNRAS, 446, 521
Schiminovich D., et al., 2007, ApJS, 173, 315
Schruba A., et al., 2011, AJ, 142, 37
Scoville N., et al., 2014, ApJ, 783, 84
Seibert M., et al., 2012, in American Astronomical Society Meeting Abstracts #219. p. 340.01
Smith D. J. B., et al., 2011, MNRAS, 416, 857
Smith D. J. B., et al., 2012, MNRAS, 427, 703
Steinacker J., Baes M., Gordon K. D., 2013, ARA&A, 51, 63
Sulentic J. W., Arp H., 1983, AJ, 88, 489
Sutherland W., 2012, in Science from the Next Generation Imaging and Spectroscopic Surveys.
Taylor M. B., 2005, in Shopbell P., Britton M., Ebert R., eds, Astronomical Society of the Pacific Conference Series Vol. 347, Astronomical Data Analysis Software and Systems XIV. p. 29
Tonry J. L., Blakeslee J. P., Ajhar E. A., Dressler A., 2000, ApJ, 530, 625
Valiante E., et al., 2016, preprint, (arXiv:1606.09615)
Verley S., et al., 2010, A&A, 518, L68
Viaene S., et al., 2014, A&A, 567, A71
Viaene S., et al., 2016, A&A, 586, A13
Vogelsberger M., et al., 2014, MNRAS, 444, 1518
Walt S. v. d., Colbert S. C., Varoquaux G., 2011, Computing in Science & Engineering, 13, 22
Walter F., Brinks E., de Blok W. J. G., Bigiel F., Kennicutt Jr. R. C., Thornley M. D., Leroy A., 2008, AJ, 136, 2563
Wenger M., et al., 2000, A&AS, 143, 9
Werner M. W., et al., 2004, ApJS, 154, 1
Wong T., Blitz L., 2002, ApJ, 569, 157
Wong O. I., et al., 2006, MNRAS, 371, 1855
Wright E. L., et al., 2010, AJ, 140, 1868
Yin J., Hou J. L., Prantzos N., Boissier S., Chang R. X., Shen S. Y., Zhang B., 2009, A&A, 505, 497
Zhukovska S., 2014, A&A, 562, A76
Zwaan M. A., et al., 2004, MNRAS, 350, 1210
da Cunha E., Charlot S., Elbaz D., 2008, MNRAS, 388, 1595
da Cunha E., Eminian C., Charlot S., Blaizot J., 2010, MNRAS, 403, 1894

APPENDIX A: EXCEPTIONS TO THE APERTURE PHOTOMETRY

A1 IRAS SCANPI photometry

We used the Scan Processing and Integration Tool (SCANPI[23]), following the procedure of Sanders et al. (2003) to measure 60 μm fluxes and uncertainties for our sources. For a third of the sample, no reliable detection could be found at the location of the source. For these sources the scans were inspected manually and an upper limit was defined for the flux as 3 times the local rms.

A2 *Herschel* PACS photometry

We dealt with PACS photometry as described in C15, using apertures based on the 250μm source size. In contrast to C15, we use the H-ATLAS DR1 Nebulised[24] maps for all our sources. The filtering applied to the maps could lead to a localised negative background for very extended sources (Valiante et al., 2016). By limiting the PACS aperture to the obvious extent of the dust emission we are minimising the effects of these large scale background issues and increasing the accuracy and reliability of the flux measurements. Where we do not have a strong enough 250 μm detection to reliably determine an aperture, we use an aperture 0.8 times the largest aperture size from the other bands. This factor was determined to be the average ratio of $\mathrm{r_{ap(250)}}/\mathrm{r_{ap(max)}}$ for sources with $\mathrm{SNR_{250}} > 5$ within the aperture. We have performed tests that there are no significant systematic differences in the fluxes obtained when either using a larger aperture or when the raw Scanamorphos (Roussel, 2013) maps are used instead.

APPENDIX B: PROPERTIES OF THE HIGH GALAXIES

Basic properties for our HI-selected sample, such as identifiers, positions and sizes are given in Table B1. The HI fluxes, HI masses, references and other HI-derived properties are given in Table B2. The UV to FIR photometry for the HI-selected HIGH sample can be found in Table B3. Multiwavelength imagery of the HIGH galaxies is shown in Figure B1 . The MAGPHYS fits to the spectral energy distributions of the HIGH sources are shown in Figure B2.

[23] Provided by the NASA/IPAC Infrared Science Archive: http://irsa.ipac.caltech.edu/applications/Scanpi/
[24] Nebuliser is an algorithm to remove background emission (Irwin, 2010)

Table B1. Basic properties for our HI-selected sample. Velocities and distances are corrected for bulk deviation from Hubble flow (Baldry et al., 2012). Semi major axes were calculated using the bespoke photometry pipeline (See Section 2.3 and C15). HAPLESS ID (C15) given for overlapping sources.

#	Common name	HIPASS ID	H-ATLAS IAU ID	HAPLESS	RA (J200 deg)	DEC (J200 deg)	z (helio)	velocity (km s^{-1})	Distance (Mpc)	Semi-maj (")
1	SDSSJ084258.35+003838.5	HIPASSJ0842+00	HATLASJ084258.4+003838		130.74318	0.64408	0.03464	10696	158.9	36.4
2	UGC04673	HIPASSJ0855+02	HATLASJ085552.3+023125		133.967	2.52426	0.01277	4020	59.7	77.2
3	UGC04684	HIPASSJ0856+00	HATLASJ085640.5+002229	39	134.17066	0.37591	0.00859	2730	40.6	62.4
4[a,b]	UGC04996	HIPASSJ0923-00	HATLASJ092315.6-004342		140.81604	-0.72945	0.01174	3852	57.3	72.6
5	UGC06578	HIPASSJ1136+00b	HATLASJ113636.7+004901	41	174.153	0.81678	0.00378	1374	20.4	56.8
6	UGC06780	HIPASSJ1148-02	HATLASJ114850.4-020156	19	177.20993	-2.03249	0.00578	2298	34.2	135.0
7[a]	UM456	HIPASSJ1150-00	HATLASJ115036.2-003406	17	177.65105	-0.56613	0.00574	2270	33.7	40.3
8[a]	UM456A	HIPASSJ1150-00	HATLASJ115033.8-003213	24	177.6415	-0.53795	0.006	2391	35.5	32.1
9	UGC06903	HIPASSJ1155+01	HATLASJ115536.9+011417	31	178.9025	1.23817	0.00635	2534	37.7	109.4
10	UGC06970	HIPASSJ1158-01			179.69101	-1.46169	0.005	2040	30.3	72.6
11	NGC4030b	HIPASSJ1200-00			180.19873	-0.02333	0.0065	2581	38.4	73.1
12	NGC4030	HIPASSJ1200-01	HATLASJ120023.7-010553	6	180.09841	-1.10033	0.00477	1978	29.4	180.7
13	UGC07053	HIPASSJ1204-01			181.0863	-1.53071	0.00488	2028	30.1	85.3
14	UGC07332	HIPASSJ1217+00			184.48653	0.43491	0.00318	936	13.9	109.8
15[a]	NGC4202	HIPASSJ1218-01	HATLASJ121808.4-010350		184.53574	-1.06413	0.019	6272	93.2	62.4
16[a]	FGC1412	HIPASSJ1220+00			184.85783	0.21197	0.00302	761	11.3	48.5
17[a]	CGCG014-010	HIPASSJ1220+00			185.08868	0.36769	0.00306	796	11.8	60.9
18	UGC07394	HIPASSJ1220+01	HATLASJ122027.6+012812	11	185.11652	1.46789	0.00526	2197	32.6	81.2
19[a]	UGC07531	HIPASSJ1226-01	HATLASJ122611.1-011813	34	186.55054	-1.30325	0.00675	2654	39.4	32.5
20[a]	UM501	HIPASSJ1226-01			186.59463	-1.2534	0.00676	2658	39.5	32.5
21	NGC5496	HIPASSJ1411-01	HATLASJ141137.7-010928	7	212.9082	-1.15909	0.00488	1840	27.4	174.8
22	NGC5584	HIPASSJ1422-00	HATLASJ142223.4-002313	14	215.59857	-0.3869	0.00548	2033	30.2	154.3
23	UGC09215	HIPASSJ1423+01	HATLASJ142327.2+014335	3	215.86342	1.7243	0.00457	1726	25.6	124.5
24[a]	SDSSJ142653.06+005746.2	HIPASSJ1427+00	HATLASJ142653.0+005745		216.72078	0.96285	0.02618	8099	120.4	62.4
25[a]	IC1011	HIPASSJ1427+00	HATLASJ142804.4+010023		217.01885	1.00607	0.02564	7938	118.0	62.4
26[a]	IC1010	HIPASSJ1427+00	HATLASJ142720.5+010132		216.83483	1.02589	0.02566	7954	118.2	93.5
27	UGC09299	HIPASSJ1429-00	HATLASJ142934.8-000105	9	217.39393	-0.01906	0.00516	1904	28.3	113.8
28	SDSSJ143353.30+012905.6	HIPASSJ1433+01			218.47167	1.48543	0.00609	2220	33.0	60.9
29	NGC5690	HIPASSJ1437+02	HATLASJ143740.9+021729	23	219.42	2.29162	0.00583	2160	32.1	154.3
30	NGC5691	HIPASSJ1437-00	HATLASJ143753.3-002354	28	219.47216	-0.39846	0.00626	2244	33.4	78.5
31	UGC09432	HIPASSJ1439+02			219.766	2.94708	0.00513	1920	28.5	69.0
32[a]	NGC5705	HIPASSJ1439-00	HATLASJ143949.5-004305	26	219.95623	-0.71874	0.00589	2110	31.4	117.8
33	NGC5725	HIPASSJ1440+02			220.24298	2.18655	0.00543	1980	29.4	52.7
34[a]	NGC5713	HIPASSJ1440-00	HATLASJ144011.1-001725	29	220.04759	-0.28933	0.00633	2260	33.6	124.5
35[a]	NGC5719	HIPASSJ1440-00	HATLASJ144056.2-001906	20	220.23393	-0.31856	0.00575	2067	30.7	171.0
36[a]	UGC09482	HIPASSJ1442+00	HATLASJ144247.1+003942		220.69539	0.66151	0.00606	2179	32.4	65.0
37[a]	UGC09470	HIPASSJ1442+00	HATLASJ144148.7+004121	30	220.45274	0.68756	0.00637	2290	34.0	60.9
38[a]	NGC5740	HIPASSJ1444+01	HATLASJ144424.3+014046	10	221.10171	1.68019	0.0052	1890	28.1	139.4
39[c]	UGC0700		HATLASJ120110.4-011750	8	180.295	-1.29751	0.00501	2070	30.8	69.1
40[c]	NGC5746		HATLASJ144455.9+015719	21	221.23292	1.955	0.00575	2070	30.8	276.6

[a] The HIPASS signal for this source is confused. Higher resolution HI data from ALFALFA or the literature were supplemented to resolve confusion. Note that only unconfused counterparts are listed in this table.
[b] Based on its colour, stellar mass and position, we identified this galaxy as the likely source of most of the HI flux in HIPASSJ0923-00.
[c] UGC0700 and NGC5746 are both sources that are bright enough to make it into HIPASS and our sample, yet they were missed in HIPASS due to their close proximity to other, brighter HIPASS sources.

Table B2. HI Properties for all the sources in the HI-selected HIGH sample. The gas fraction does not include molecular gas (i.e. $f_g = M_{HI}/(M_{HI} + M_*)$. The M_{HI}/M_* and M_d/M_{HI} ratios use MAGPHYS derived stellar and dust masses (See Table 1).

#	common name	S_{int} (Jy km/s)	log M_{HI} ($M_\odot$)	gas fraction	log M_{HI}/M_*	log M_d/M_{HI}	HI origin
1[c]	SDSSJ084258.35+003838.5	1.56	9.97	0.58	0.14	-2.81	ALFALFA
2	UGC04673	7.18	9.78	0.82	0.67	-2.41	ALFALFA
3	UGC04684	9.72	9.58	0.63	0.23	-2.91	ALFALFA
4[a,b]	UGC04996	9.00	9.84	0.75	0.48	-2.71	HIPASS
5	UGC06578	6.72	8.82	0.86	0.8	-3.11	ALFALFA
6	UGC06780	26.90	9.87	0.88	0.87	-2.94	HIPASS
7[a]	UM456	2.86	8.89	0.8	0.6	-3.93	Taylor et al. (1995)
8[a]	UM456A	2.86	8.93	0.92	1.05	-4.06	Taylor et al. (1995)
9	UGC06903	14.11	9.68	0.38	-0.21	-2.53	ALFALFA
10	UGC06970	5.20	9.05	0.31	-0.34	-2.56	HIPASS
11	NGC4030b	6.61	9.36	0.78	0.55	-3.76	ALFALFA
12	NGC4030	72.00	10.17	0.16	-0.71	-2.27	HIPASS
13	UGC07053	8.30	9.25	0.92	1.06	-4.46	HIPASS
14	UGC07332	19.61	8.95	0.95	1.25	-4.65	ALFALFA
15[a]	NGC4202	12.56	10.41	0.56	0.11	-2.97	Richer et al. (1987)
16[a]	FGC1412	2.35	7.85	0.89	0.92	-4.02	ALFALFA
17[a]	CGCG014-010	4.87	8.21	0.89	0.93	-4.74	ALFALFA
18	UGC07394	6.86	9.24	0.67	0.31	-2.4	ALFALFA
19[a]	UGC07531	3.05	9.05	0.74	0.45	-2.58	Taylor et al. (1995)
20[a]	UM501	6.60	9.39	0.97	1.49	-4.31	Taylor et al. (1995)
21	NGC5496	60.90	10.03	0.79	0.58	-2.95	HIPASS
22	NGC5584	27.10	9.76	0.38	0.76	-2.3	HIPASS
23	UGC09215	23.18	9.56	0.64	0.25	-2.64	ALFALFA
24[a,c]	SDSSJ142653.06+005746.2	1.23	9.62	0.52	0.03	-2.4	ALFALFA
25[a,c]	IC1011	1.62	9.73	0.27	-0.43	-2.34	ALFALFA
26[a]	IC1010	10.80	10.55	0.36	-0.26	-2.65	ALFALFA
27	UGC09299	45.54	9.94	0.95	1.32	-3.57	ALFALFA
28	SDSSJ143353.30+012905.6	3.42	8.94	0.94	1.18	-4.43	ALFALFA
29	NGC5690	32.97	9.9	0.25	-0.48	-2.33	ALFALFA
30	NGC5691	5.50	9.16	0.12	-0.85	-2.33	HIPASS
31	UGC09432	8.03	9.19	0.91	1.0	-4.8	ALFALFA
32[a]	NGC5705	25.30	9.77	0.73	0.44	-2.46	Fisher et al. (1981)
33	NGC5725	4.20	8.93	0.39	-0.2	-2.53	ALFALFA
34[a]	NGC5713	42.79	10.06	0.24	-0.5	-2.55	Schneider et al. (1986)
35[a]	NGC5719	52.45	10.07	0.16	-0.72	-2.67	Schneider et al. (1986)
36[a]	UGC09482	5.86	9.16	0.74	0.45	-3.1	ALFALFA
37[a]	UGC09470	4.84	9.12	0.62	0.22	-2.94	ALFALFA
38[a]	NGC5740	29.23	9.74	0.22	-0.54	-2.61	ALFALFA
39[d]	UGC0700	5.7	9.1	0.5	-0.01	-2.7	Sulentic et al. (1983)
40[d]	NGC5746	30.7	9.84	0.03	-1.47	-1.87	Popping et al. (2011)
Mean		16.25	9.46	0.61	0.28	-3.05	
$M_* < 10^9$		9.72	9.07	0.87	0.87	-3.74	
$M_* > 10^9$		21.33	9.76	0.44	-0.09	-2.56	

[a] The HIPASS signal for this source is confused. Higher resolution HI data from ALFALFA or the literature were supplemented to resolve confusion. Note that only unconfused counterparts are listed in this table.
[b] Based on its colour, stellar mass and position, we identified this galaxy as the likely source of most of the HI flux in HIPASSJ0923-00.
[c] The individual HI-flux is lower than HIPASS detection limit.
[d] UGC0700 and NGC5746 are both sources that are bright enough to make it into HIPASS and our sample, yet they were missed in HIPASS due to their close proximity to other, brighter HIPASS sources.

Table B3. Photometry for the HI-selected sample. UV-IR photometry has been corrected for Galactic extinction in line with Adelman-McCarthy et al. (2008). The *Herschel*-SPIRE fluxes were measured using maps reduced for extended sources, but have not been colour-corrected. The given uncertainties do not include calibration uncertainties. Before fitting an SED, we have added in quadrature the calibration error or 10 per cent, whichever is larger. The semi-major axis of the aperture is denoted by a, the position angle by θ (east of north) and the axial ratio by a/b.

#	Common name	Aperture dimensions			*GALEX* (mJy)				SDSS (mJy)							
		a(arcsec)	θ (deg)	a/b	FUV	ΔFUV	NUV	ΔNUV	u	Δu	g	Δg	r	Δr	u	Δu
1	SDSSJ084258.35+003838.5	36.56	2.91	1.33	0.211	0.004	0.265	0.023	0.59	0.36	1.37	0.13	1.97	0.15	2.63	0.35
2	UGC04673	77.27	-10.73	1.2	1.061	0.011	1.390	0.051	0.46	1.06	4.86	0.65	5.93	1.00	6.73	1.81
3	UGC04684	60.99	42.35	1.05	1.938	0.007	2.533	0.051	3.33	0.94	9.56	0.51	12.99	0.72	16.13	0.99
4	UGC04996	60.99	30.86	1.53	1.304	0.006	1.877	0.017	3.04	0.37	7.12	0.27	9.25	0.41	10.19	0.83
5	UGC06578	56.92	43.02	1.41	1.812	0.005	2.067	0.006	2.74	0.76	5.07	0.23	5.80	0.25	6.39	0.59
6	UGC06780	125.97	107.49	2.8	-	-	2.790	0.022	5.00	1.28	11.97	0.55	14.35	0.83	17.06	1.61
7	UM456	40.58	91.72	1.16	0.978	0.004	1.189	0.011	1.76	0.16	3.34	0.24	3.88	0.46	3.92	0.97
8	UM456A	32.42	-13.84	1.87	0.284	0.002	0.321	0.004	0.48	0.07	0.94	0.10	1.16	0.18	1.17	0.33
9	UGC06903	105.75	46.69	1.16	2.875	0.011	3.016	0.064	4.38	3.31	19.49	1.02	28.01	1.91	34.10	3.91
10	UGC06970	65.06	-10.33	1.42	1.081	0.008	1.491	0.017	3.20	2.03	7.82	0.56	13.15	0.38	22.51	0.82
11	NGC4030b	73.2	15.52	1.12	0.644	0.005	0.781	0.015	0.98	1.42	3.60	0.17	5.30	0.49	6.55	1.44
12	NGC4030	170.84	134.08	1.41	11.979	0.031	22.401	0.027	56.87	3.58	191.95	1.99	327.87	2.71	447.49	4.62
13	UGC07053	85.4	102.19	1.56	0.610	0.007	0.801	0.014	1.72	1.65	3.08	0.38	3.64	1.12	4.07	1.32
14	UGC07332	109.82	16.85	1.09	1.682	0.013	2.039	0.020	3.15	1.31	6.72	1.70	3.63	2.03	8.93	2.05
15	NGC4202	56.92	49.65	1.88	0.282	0.006	0.749	0.012	2.64	0.10	7.46	0.20	12.90	0.26	17.02	0.45
16	FGC1412	52.81	98.99	3.57	0.188	0.002	0.243	0.004	0.41	0.09	0.86	0.05	1.01	0.07	1.14	0.22
17	CGCG014-010	60.99	-42.33	2.73	0.414	0.004	0.551	0.013	0.83	0.16	1.80	0.06	1.93	0.09	2.29	0.23
18	UGC07394	81.31	54.57	3.45	0.411	0.005	0.705	0.008	1.97	0.33	5.04	0.45	7.18	0.53	8.17	0.85
19	UGC07531	45.0	0.0	1.0	1.994	0.007	2.143	0.018	3.25	0.49	6.10	0.30	6.87	0.50	7.17	0.86
20	UM501	31.59	120.0	1.57	0.506	0.002	0.410	0.007	0.79	0.15	1.36	0.08	1.39	0.17	1.33	0.24
21	NGC5496	210.0	83.07	4.2	5.311	0.038	8.017	0.029	12.69	6.03	34.00	0.64	46.02	1.52	54.49	1.87
22	NGC5584	138.3	63.47	1.26	9.901	0.019	13.541	0.061	26.66	4.84	64.37	2.38	93.91	2.45	105.27	4.38
23	UGC09215	109.82	71.65	1.47	5.778	0.014	7.441	0.066	13.62	4.88	29.33	1.73	38.32	2.31	45.71	3.69
24	2MASXJ14265308+0057462	24.25	-3.35	1.38	0.175	0.003	0.260	0.010	0.60	0.09	1.65	0.05	2.27	0.08	2.47	0.12
25	IC1011	36.5	-17.74	1.14	0.687	0.004	1.105	0.006	2.32	0.20	5.35	0.15	7.95	0.25	9.85	0.33
26	IC1010	97.61	91.4	1.19	1.165	0.011	1.550	0.075	3.29	1.80	12.54	1.47	22.46	1.60	28.49	2.13
27	UGC09299	113.89	-18.47	1.53	2.492	0.029	3.114	0.051	3.89	1.06	10.65	0.64	10.68	1.19	12.89	2.36
28	SDSSJ143353.30+012905.6	60.99	98.24	2.96	0.148	0.004	0.193	0.013	0.21	0.80	0.67	0.30	0.82	0.31	0.96	0.76
29	NGC5690	122.02	60.0	2.32	1.994	0.014	3.811	0.143	13.17	2.79	42.80	4.03	71.51	5.20	98.39	3.55
30	NGC5691	60.99	63.13	1.16	2.079	0.007	3.285	0.033	14.31	1.14	36.52	0.49	53.98	0.56	65.48	1.04
31	UGC09432	69.13	-44.31	1.2	0.890	0.006	1.042	0.019	1.86	1.85	3.82	0.75	4.28	0.95	4.23	1.12
32	NGC5705	117.94	-20.27	1.38	4.186	0.016	5.362	0.036	5.61	3.34	23.41	1.24	35.32	1.84	42.05	2.11
33	NGC5725	52.85	117.69	1.14	1.573	0.008	2.222	0.014	4.25	0.63	9.59	0.29	13.38	0.53	15.67	0.88
34	NGC5713	89.49	92.25	1.17	4.667	0.015	9.649	0.039	33.50	2.05	95.45	0.95	157.65	1.42	201.46	1.92
35	NGC5719	185.0	29.36	4.11	0.508	0.020	0.992	0.041	10.16	1.75	41.36	0.82	95.67	2.2	146.43	3.80
36	UGC09482	65.06	-22.6	3.2	0.409	0.004	0.635	0.005	1.47	0.39	3.36	0.09	4.72	0.15	5.60	0.29
37	UGC09470	60.99	-42.57	1.47	1.243	0.009	1.578	0.011	3.00	0.55	6.12	0.36	8.31	0.41	9.37	0.92
38	NGC5740	126.08	63.69	2.16	3.154	0.014	4.986	0.019	11.58	4.01	47.29	0.31	84.12	1.16	112.22	0.97
39	UGC07000	69.1	-29.7	1.39	2.617	0.007	3.286	0.011	5.94	1.18	11.99	0.62	15.68	0.87	19.12	1.05
40	NGC5746	276.61	78.56	4.49	-	-	-	-	32.63	5.29	137.90	2.34	323.15	2.77	496.51	7.12

Table B3. - *continued*

#	VIKING (mJy)										WISE (mJy)							
	Z	ΔZ	Y	ΔY	J	ΔJ	H	ΔH	K_S	ΔK_S	3.4μm	Δ3.4μm	4.6μm	Δ4.6μm	12μm	Δ12μm	22μm	Δ22μm
1	2.76	0.69	3.20	0.96	3.33	0.48	3.54	1.77	2.72	1.04	1.64	0.26	0.97	0.24	2.29	0.66	4.45	1.90
2	6.87	1.66	6.51	2.58	6.29	2.70	2.58	8.06	4.80	1.83	4.75	0.98	3.03	0.84	4.47	1.88	13.97	3.92
3	22.35	3.53	20.38	2.93	21.82	3.44	18.09	1.21	16.17	1.81	-	-	-	-	-	-	-	-
4	11.39	0.54	12.70	0.56	13.30	0.59	11.72	2.86	11.52	0.66	4.95	0.53	3.40	0.38	9.32	0.79	15.93	3.68
5	7.20	0.40	6.21	1.29	6.73	1.43	2.62	1.50	2.95	1.82	3.82	0.44	2.38	0.34	8.56	1.07	42.56	3.42
6	15.95	1.02	13.51	1.64	19.49	1.81	18.41	4.37	11.54	3.36	9.73	0.63	5.16	0.83	5.57	1.02	21.24	4.19
7	4.18	0.67	4.39	1.20	4.37	1.79	4.31	2.2	3.13	1.07	1.46	0.71	1.03	0.48	1.70	0.82	15.35	2.24
8	1.23	0.16	1.23	0.33	1.37	0.48	1.32	0.68	1.29	0.71	0.58	0.35	0.20	0.26	0.51	0.41	5.41	1.65
9	44.43	7.06	47.44	4.50	49.94	7.47	51.89	4.71	40.11	4.46	23.03	3.44	14.66	2.72	31.08	1.87	26.26	6.79
10	23.01	0.38	24.74	0.48	25.27	0.71	24.81	1.62	24.31	1.09	-	-	-	-	-	-	-	-
11	6.13	0.75	6.58	0.58	6.21	0.87	6.58	2.00	5.35	2.31	3.09	0.87	2.08	0.73	1.85	1.62	-1.32	5.94
12	543.82	2.68	667.79	4.32	759.13	4.85	900.11	5.07	759.58	6.35	458.13	2.41	285.00	1.40	1283.52	3.56	1936.21	9.48
13	2.67	1.01	2.41	1.40	4.13	1.70	3.18	4.00	2.75	1.29	2.26	0.52	1.99	0.79	-1.02	1.38	12.11	4.6
14	5.87	0.76	6.16	1.64	10.54	3.83	6.88	4.18	1.13	3.70	3.93	1.15	3.43	2.76	10.64	11.69	-75.52	26.70
15	20.20	0.40	24.48	0.64	27.06	0.57	30.77	0.75	26.62	1.03	14.32	0.25	8.69	0.37	32.78	2.11	43.17	4.51
16	1.37	0.11	1.47	0.20	1.41	0.26	-	-	1.13	0.81	0.47	0.16	0.16	0.23	0.18	1.49	10.27	4.44
17	2.71	0.12	2.77	0.17	2.80	0.20	-	-	2.16	1.00	1.14	0.18	0.31	0.42	-0.17	3.80	-2.09	4.57
18	10.07	0.30	11.07	0.55	11.31	0.95	17.30	4.25	9.45	2.26	4.87	0.41	2.95	0.95	4.72	3.16	10.63	4.9
19	7.11	0.97	7.28	0.70	7.26	1.08	7.22	0.99	5.76	0.79	2.93	0.48	1.81	0.43	3.84	0.73	13.99	2.97
20	1.34	0.15	1.36	0.34	1.28	0.54	1.22	0.40	0.98	0.41	0.71	0.14	0.36	0.16	0.24	0.41	10.64	1.76
21	-	-	-	-	55.54	2.42	80.08	4.97	45.65	1.81	36.09	0.70	22.83	0.67	41.49	1.64	64.31	5.39
22	121.54	2.49	130.23	2.83	129.62	2.82	131.19	8.34	117.33	3.82	72.53	2.27	45.16	1.34	159.81	3.65	330.71	5.27
23	49.26	4.24	53.24	2.96	55.53	4.9	54.45	3.73	38.67	4.22	28.14	2.58	17.87	1.34	51.30	1.28	117.04	3.86
24	3.34	0.16	3.81	0.21	4.11	0.40	4.16	0.57	3.99	0.34	1.97	0.15	1.28	0.12	5.86	0.23	13.65	0.84
25	11.88	0.65	13.82	0.87	15.34	0.60	17.52	0.59	14.30	0.54	9.14	0.22	5.87	0.19	34.00	0.40	56.25	1.86
26	23.99	3.54	39.29	9.35	40.06	5.66	52.65	4.94	37.98	4.64	24.35	3.72	13.72	2.79	24.67	1.67	27.05	3.52
27	11.60	4.54	12.65	4.38	11.81	4.55	4.20	6.19	5.87	5.71	5.66	1.56	3.16	1.99	7.87	1.23	22.07	5.33
28	1.09	0.39	1.15	0.43	1.18	0.71	0.95	1.18	1.62	2.38	0.38	0.30	-0.20	0.28	0.23	0.56	-0.54	1.98
29	125.93	2.74	157.51	2.91	179.73	2.73	221.01	4.33	190.26	7.66	118.96	1.04	77.84	0.82	399.63	2.74	609.96	4.34
30	76.51	0.78	86.41	1.16	92.99	0.81	102.01	1.32	80.4	2.68	47.70	0.67	30.55	0.49	130.42	0.76	304.88	3.10
31	4.53	1.71	3.34	1.67	4.95	1.38	-10.54	2.21	3.74	2.75	2.00	0.82	0.59	0.59	0.54	0.79	0.94	3.10
32	42.30	0.79	42.46	1.29	41.18	1.23	32.60	1.73	29.97	4.17	22.93	0.65	14.21	0.75	26.47	1.38	33.35	4.65
33	17.51	0.43	19.16	0.62	20.46	0.85	23.72	1.19	17.08	1.06	10.47	0.33	6.33	0.44	17.79	0.63	24.98	2.42
34	241.54	1.43	288.94	1.75	325.88	2.22	370.08	1.85	312.09	11.10	190.49	0.90	129.90	0.77	914.84	1.71	2362.8	4.81
35	193.50	5.43	256.49	6.77	319.21	3.52	399.96	3.57	345.82	12.40	191.03	3.69	116.08	2.18	373.55	2.2	679.42	5.66
36	6.18	0.21	6.60	0.33	6.80	0.24	7.15	0.47	5.58	0.55	2.60	0.21	1.62	0.21	1.61	0.44	7.30	1.62
37	10.16	0.44	10.31	0.52	10.31	0.52	9.98	1.86	8.71	1.14	5.05	0.40	2.69	0.47	2.84	0.46	12.77	1.77
38	143.49	0.46	173.28	0.49	197.03	0.86	228.03	0.90	178.12	1.62	101.88	0.53	58.83	0.59	181.98	0.96	327.74	3.64
39	19.76	1.76	21.22	2.04	22.54	1.80	25.29	2.38	19.25	2.60	11.33	0.49	7.15	0.62	15.52	1.05	27.18	3.64
40	673.93	18.87	910.96	20.16	1124.89	17.99	1401.90	26.53	1219.78	19.23	622.88	16.93	347.73	10.10	391.11	4.71	429.59	5.20

Table B3. - *continued*

#	IRAS SCANPI (mJy)		*Herschel*-PACS (mJy)				*Herschel*-SPIRE (mJy)					
	60 μm	Δ60 μm	100 μm	Δ100 μm	160 μm	Δ160 μm	250 μm	Δ250 μm	350 μm	Δ350 μm	500 μm	Δ500 μm
1	140.0[a]	-38.7[a]	114.0	120.4	146.0	105.9	103.6	28.5	63.8	26.4	21.1	19.9
2	60.0	60.0	207.1	207.3	302.2	158.8	317.5	58.8	215.6	46.5	132.0	32.8
3	350.0	129.6	851.1	200.1	1006.2	157.4	563.3	45.4	280.8	40.2	126.5	26.6
4	340.0	111.8	876.8	195.7	775.5	145.7	542.0	37.2	313.7	33.1	131.7	27.6
5	380.0	132.6	262.8	121.4	231.7	98.0	188.8	39.1	97.9	35.8	52.9	24.2
6	160.0	85.4	228.8	186.8	370.8	144.2	393.7	51.6	267.2	43.6	133.2	33.4
7	110.0	67.8	228.0	148.1	58.9	119.7	49.1	32.3	18.3	29.9	8.9	23.8
8	350.0[a]	-99.8[a]	4.3	87.1	133.7	84.2	33.3	22.7	13.7	21.4	-4.8	20.0
9	310.0	111.0	1120.0[b]	98.0[b]	2739.7	288.8	1349.2	63.7	808.6	49.3	327.3	38.7
10	280.0	119.2	127.9	198.4	371.4	163.0	406.1	42.0	220.5	35.2	96.1	26.5
11	190.0[a]	-57.5[a]	227.6	264.6	499.0	213.1	76.5	52.8	78.1	45.4	18.8	33.4
12	16550.0	3376.4	60459.7	479.0	70131.2	362.0	33414.7	93.8	13566.3	70.7	4556.4	51.4
13	141.3[a]	-47.1[a]	253.5	292.9	306.7	249.4	28.3	48.4	5.2	41.5	-10.0	31.7
14	140.0	77.5	159.5	491.8	122.7	361.9	3.3	69.7	-4.2	61.6	78.7	46.2
15	290.0	124.0	1455.2	220.0	1910.3	195.2	996.9	32.0	410.4	28.7	146.1	21.6
16	156.9[a]	-52.3[a]	81.8	117.6	-30.6	98.6	17.8	25.7	17.7	25.7	35.1	20.1
17	160.1[a]	-53.4[a]	87.3	148.3	-38.3	127.9	-34.6	33.5	-28.3	28.2	-28.5	22.9
18	-	-	260.7	143.7	385.3	125.8	260.5	32.9	206.1	29.1	126.0	22.6
19	260.0	68.0	141.7	180.5	139.6	156.1	138.7	32.8	88.6	30.0	67.0	21.5
20	-	-	63.9	93.9	7.3	84.8	42.4	20.4	21.6	21.2	14.7	16.4
21	1000.0	268.8	2992.0	322.3	3283.1	269.0	2466.9	72.9	1373.4	63.4	636.2	51.2
22	2345.0	519.9	7795.4	505.4	8443.8	423.0	5770.6	77.2	2940.0	62.8	1180.2	53.1
23	1420.0	327.9	2768.1	341.9	3759.4	271.6	2049.2	66.7	1159.7	55.1	503.4	43.9
24	210.0	81.6	328.2	107.7	374.4	87.9	228.2	21.5	121.7	19.4	55.9	16.4
25	780.0	208.3	1501.2	138.1	1632.1	122.0	696.5	27.1	281.9	25.5	99.4	19.5
26	310.0[a]	-50.6[a]	1066.2	207.8	927.0	180.6	913.9	66.8	433.1	58.1	187.3	39.1
27	230.0	86.6	540.4	159.1	779.9	139.5	487.4	55.1	263.6	49.0	132.5	39.7
28	184.8[a]	-61.6[a]	3.1	146.1	43.1	124.1	9.1	27.4	7.0	25.7	6.9	21.6
29	6460.0	1336.3	18807.2	429.2	22254.8	375.0	11158.0	52.2	4901.4	48.3	1759.8	37.7
30	3480.0	796.3	7906.1	310.9	6943.5	221.5	2772.8	38.1	1166.0	33.3	412.6	22.9
31	159.4[a]	-53.1[a]	-	-	-	-	9.5	40.5	-38.2	34.0	-26.3	25.7
32	440.0	129.6	1325.0	378.5	2188.6	310.7	1787.3	65.9	1041.4	64.7	542.4	43.4
33	430.0	126.0	-	-	-	-	617.5	36.4	299.7	30.1	108.8	24.7
34	21290.0	4326.3	43106.1	376.5	38327.6	356.8	15351.7	55.7	5812.5	47.3	1881.3	32.8
35	8535.0	1747.2	19072.1	356.9	19922.1	273.0	9776.1	63.8	4275.7	52.1	1500.2	37.4
36	430.7[a]	-143.6[a]	84.8	99.9	185.6	85.1	144.0	29.5	79.0	24.9	29.4	20.7
37	170.0	68.8	489.1	124.3	545.1	109.4	243.1	35.2	156.7	29.0	82.3	23.0
38	3170.0	711.0	7917.2	366.4	8956.7	305.6	4825.9	52.2	2190.6	47.7	811.2	34.6
39	370.0	137.0	973.8	174.6	1276.2	138.3	624.7	43.9	317.9	35.8	112.4	28.0
40	2600.0	570.0	12903.9	604.7	24687.9	452.6	17211.5	71.8	8278.6	57.7	3203.6	48.0

[a] Sources with no reliable detection at the location of the source are shown with a negative Δ60 μm ($= -$rms). For these sources, the scans were inspected manually and an upper limit was defined as 3 times the local rms and listed as the flux.

[b] The PACS 100μm flux poorly matched the SED for UGC06903. We have instead used the IRAS 100μm photometry from Lisenfeld et al. (2007) which has a significantly higher SNR and better matches the SED.

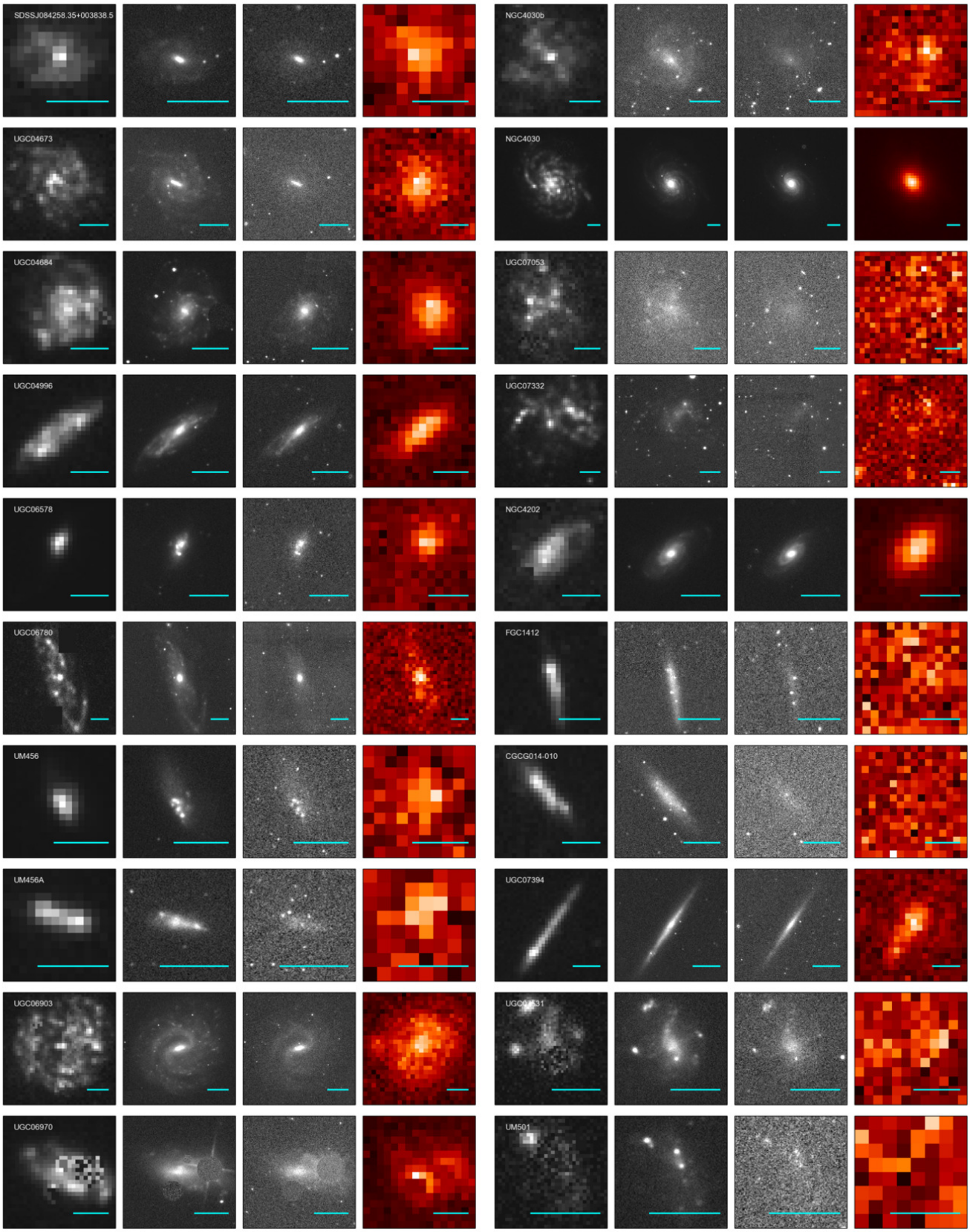

Figure B1. Multiwavelength images for all the HI-selected sources. The brightest foreground stars and background galaxies have been subtracted and replaced by adjacent pixels. The bands displayed, from left-to-right, are: *GALEX* FUV, SDSS *r*-band, VIKING K_S-band, and *Herschel* 250 μm. The size of each cutout is 1.5 times the semi-major axis of the aperture and a scale bar with a length of 30" is shown on each image in cyan.

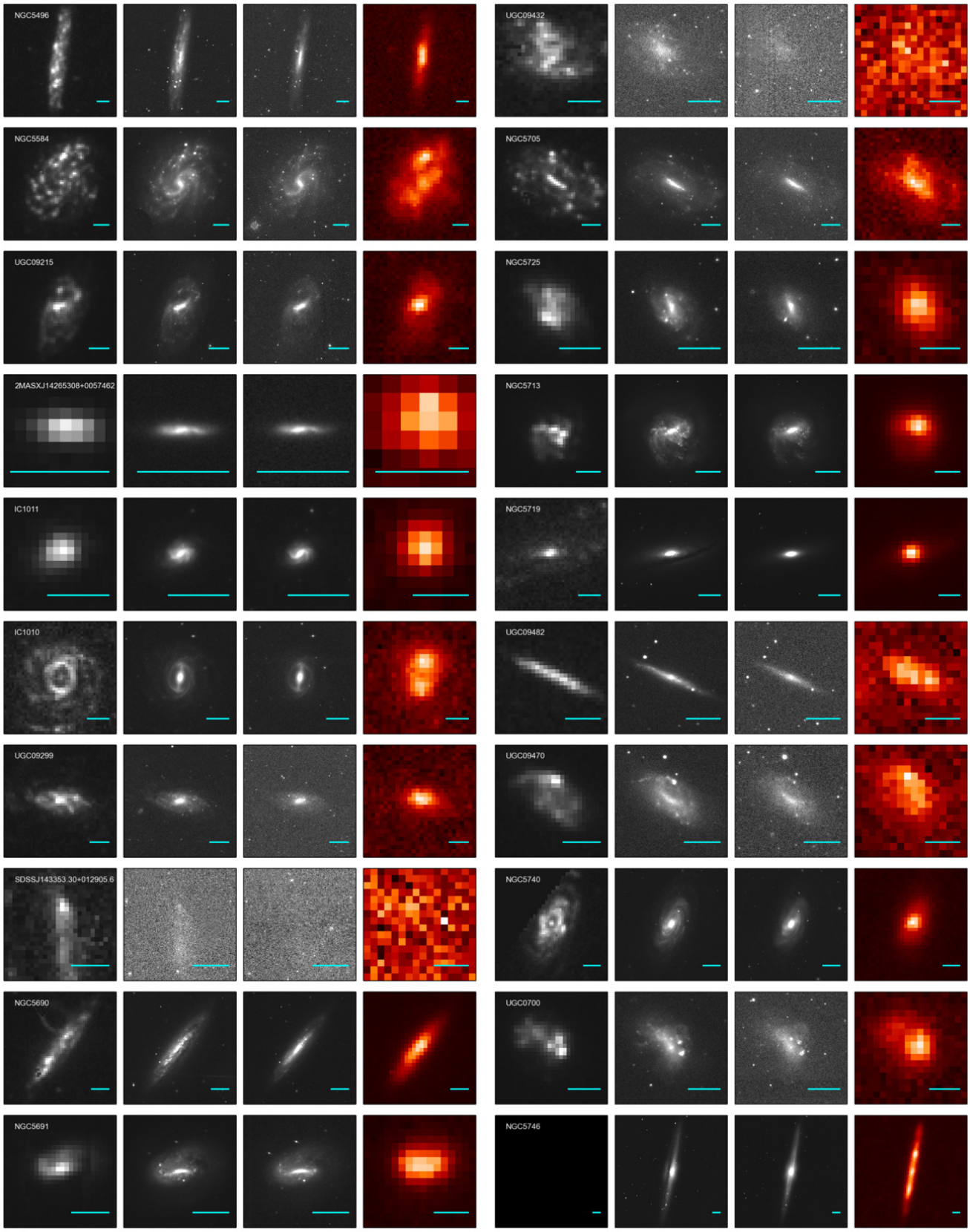

Figure B1. - *continued*

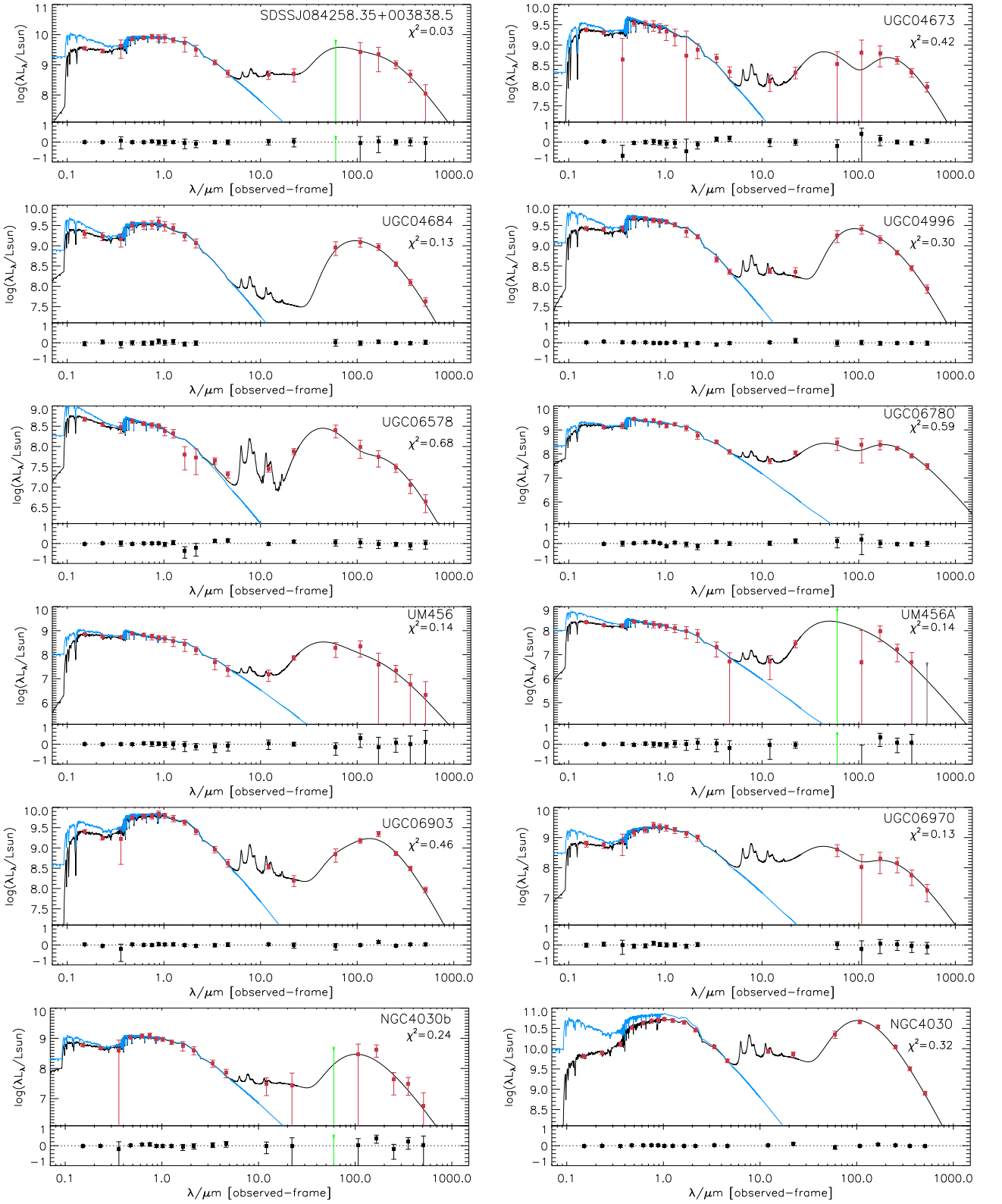

Figure B2. Multiwavelength SEDs of the 40 HI-selected sources in HIGH, with observed photometry (red points) from FUV to the submillimetre. The photometry process (including determination of errors) is described in Section 2.3. IRAS60 3σ-upper limits are shown as green triangles. Since negative fluxes cannot be plotted on a logarithmic scale, we have plotted the 1σ upper limits as orange triangles. The solid black line is the best-fit model SED and the solid blue line is the unattenuated optical model. The residuals of the fit are shown in the panel below each SED. The shown χ^2 are the total χ^2 divided by the number of bands, as given by the standard version of MAGPHYS.

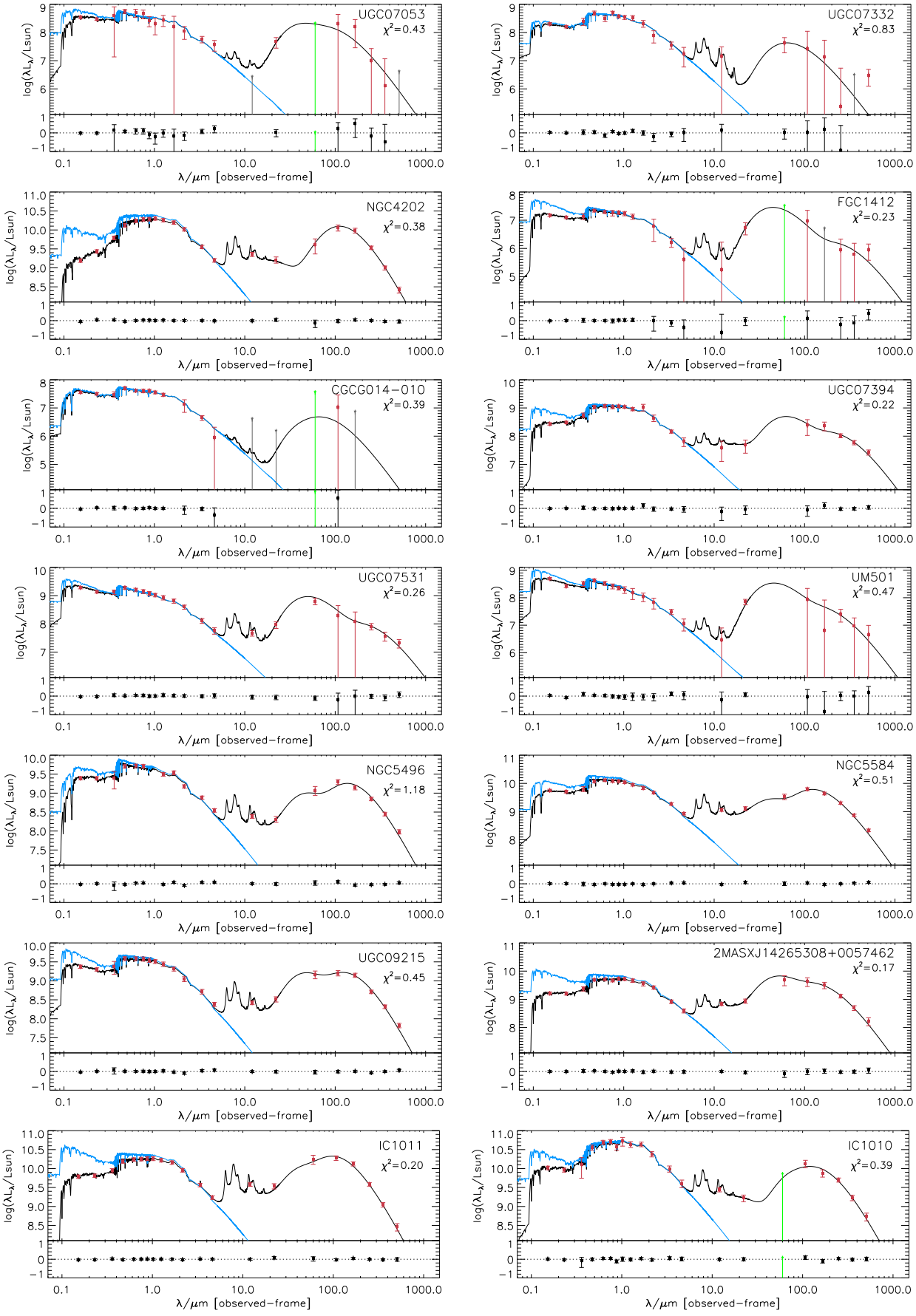

Figure B2. - *continued*

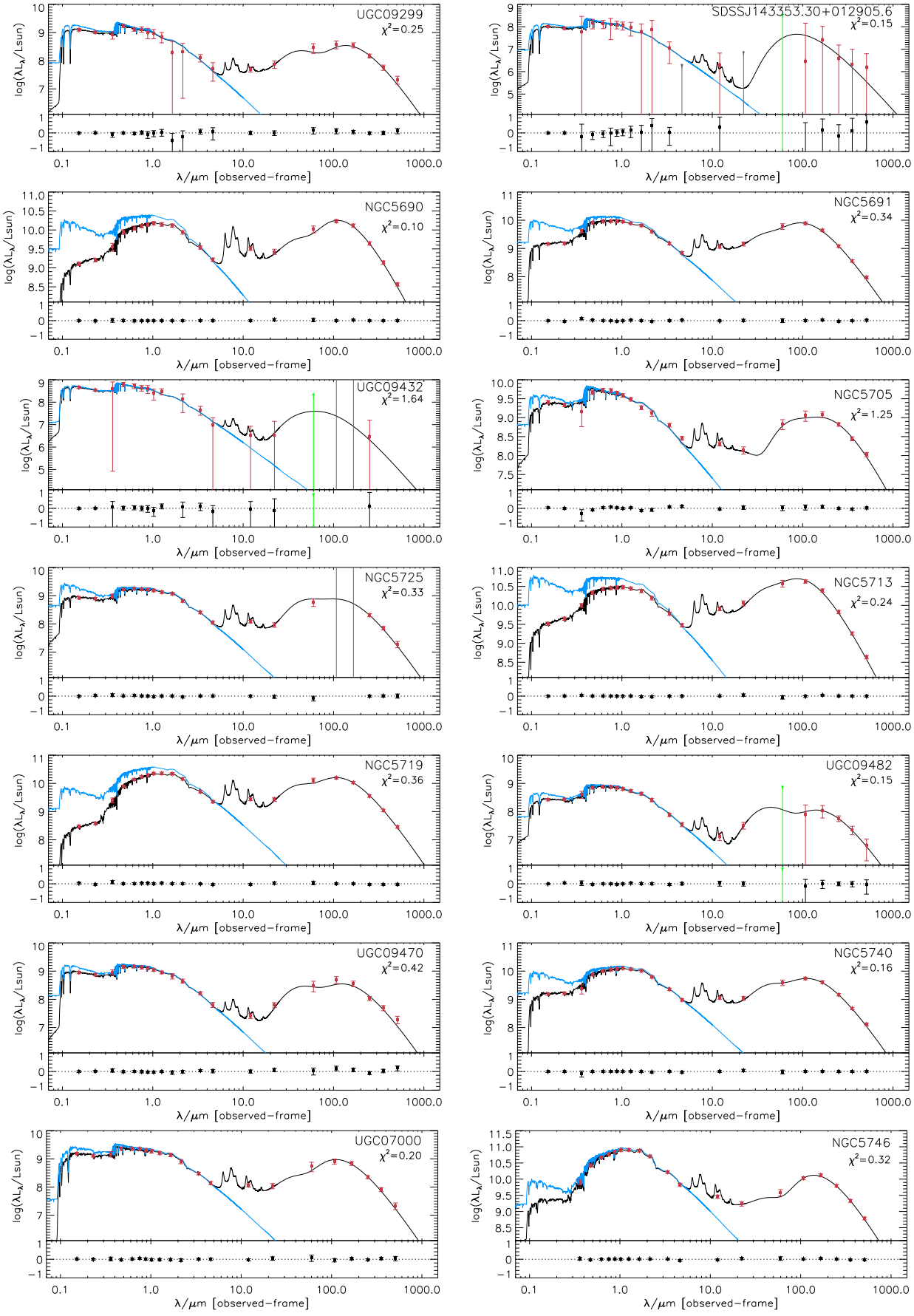

Figure B2. - *continued*